A Study Of
Space-Time Adaptive Array Processing
For
Cancellation Of GPS Jamming

by

Tri T. Phuong

Submitted to the Department of Electrical Engineering and Computer Science
in Partial Fulfillment of the Requirements for the Degrees of
Bachelor of Science in Electrical Science and Engineering
and Master of Engineering in Electrical Engineering and Computer Science
at the Massachusetts Institute of Technology

May 21st, 1999

Author_____
Department of Electrical Engineering and Computer Science
May 21st, 1999

Certified by_____
Dr. Gary F. Hatke
Thesis Supervisor

Accepted by_____
Arthur C. Smith
Chairman, Department Committee on Graduate Theses

A Study Of
Space-Time Adaptive Array Processing
For
Cancellation Of GPS Jamming

by

Tri T. Phuong

Submitted to the
Department of Electrical Engineering and Computer Science

May 21st, 1999

In Partial Fulfillment of the Requirements for the Degree of
Bachelor of Science in Electrical Science and Engineering
and Master of Engineering in Electrical Engineering and Computer Science

ABSTRACT

GPS systems operated on aircraft can easily be subjected to jamming by ground-based sources. To make matter worse, high-gain jamming signals often interact with the airframe itself creating a near-field multi-path environment. Techniques of space-time adaptive array processing are essentially the key in nulling of wide-band jammers while preserving an acceptable capability for discerning differential delay among the GPS signals. Experimental data are available for characterizing and investigating the effects of multi-path. Various space-time adaptive array algorithms are evaluated for their performances in face of these complications.

Thesis Supervisor: Dr. Gary F. Hatke
Title: Member of Staff, MIT Lincoln Laboratory

Table of Contents

List of Figures

List of Tables

1 Introduction

The Global Positioning System has become increasingly important as more aircraft and ground vehicles start to rely on the GPS satellite signals to navigate. There is no doubt that the GPS is creating many positive impacts on our everyday life as we enter the 21st century. Along with all the astounding aspects, yet, the GPS is not perfect. The GPS signal from the satellites is a very weak signal in power, thus it is easily subjected to jamming, either intentionally or unintentionally. As a result, this is a weakness of the GPS, especially for critical missions such as operations of GPS-dependent military aircraft. The good news is that the GPS signal is not totally ruined but recoverable, provided that a much more complicated anti-jamming system is available. The degrees of complexity of various anti-jamming algorithms depend on the number and types of parameters involved.

In this study, the problem is concerned with adaptive array processing for nulling wide-band jamming signals in GPS systems. Of particular interest is the case in which both a direct-path jammer as well as its near-field multi-path scatterers are all present at the array antenna mounted on an aircraft. An experiment has been conducted at Lincoln Laboratory that provides the real data for analysis of this multi-path problem. The multi-path characteristics are obtained from the real data and ultimately, will provide a better and more accurate simulation of the jamming signals. The simulated data are then used for testing several space-time adaptive array algorithms. The performance of these algorithms will be evaluated through simulations. Theoretical analysis will also be performed to obtain a better insight of the algorithm so that additional improvement can be made.

In this paper, the first section provides the readers with some background knowledge about the GPS, especially about the GPS signal characteristics. This section also includes a description of the jamming sources and signals. The significant similarities and differences between the GPS signals and the jamming signals are pointed out since these qualities are related to our ability to null out the jammers. The following chapter describes the actual experiment that has been conducted at an antenna test site to collect the data for later analysis. The objective is to show how the data have been obtained and what pre-processing should be done with the real data. A major portion of the thesis is devoted to such pre-processing, namely equalization on the real data due to channel mismatch in the receiver system. A model for the channel mismatch is proposed. Then, a method for digitally equalizing the channel is developed and evaluated for various parameters. After presenting the simulated results, the focus is shifted to the equalization of the real data. A discussion of the quality of equalization on the real data will be given. The next chapter is one of the most important chapters: forming covariance matrices out of the equalized inphase-quadrature data for each elevation angle and azimuth and plotting their eigenvalues. This chapter will present some of the plots and discuss their relationship to the multi-path effects. From the covariance matrices, it is possible to generate simulated signals being received in a particular jamming environment with multi-path effects. A discussion is devoted to showing how this is carried out. The last and most important chapter is concerned with the Space-Time Adaptive Array Algorithms for nulling wide-band jamming signals in aircraft GPS systems. The mathematics will be presented. Further analysis and interpretations of results will all be done in this final chapter.

2 Signal & Jammer Characteristics

2.1 GPS Signal Spectrum

The signal of concern is the signal being transmitted from the satellites of the Global Positioning System. In this section, the spectrum of the GPS signal will be briefly described.

The GPS signal is made up of two components: a primary signal at a center carrier frequency of 1575.42 MHz (L_1), and a secondary signal at a center carrier frequency of 1227.6 MHz (L_2). The modulating signal at both L_1 and L_2 is the 50 bps binary data multiplied by either a 1.023 MHz or a 10.23 MHz pseudo-random sequence of ±1. Accordingly, the power spectrum at each carrier frequency looks like a $\text{sinc}^2(x)$ function with a main-lobe width of either 2.046 MHz or 20.46 MHz. [1]

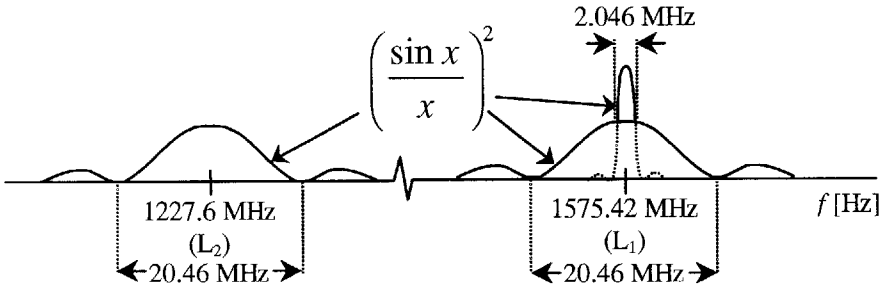

Figure 2.1: Power Spectral Density of GPS Signals

2.2 GPS Signal Power

As regards to the signal strength, the GPS signal is rather weak. The thermal white noise power substantially exceeds the signal power. For instance, a typical value for the noise power density is about –205 dBW/Hz. In contrast, the GPS signal power spectral density is only about –220 dBW/Hz for the 1.023 MHz code, and about –233

dBW/Hz for the 10.23 MHz code. [1] Thus, in normal operations, a single GPS signal is not even visible on a spectrum analyzer. For that reason, it is necessary to perform a correlation operation in order to extract the GPS data. This is possible since the pseudo-random sequence is assumed to be known and can be used as a reference signal for correlating with the received signal.

2.3 Spread Spectrum Signaling

The whole process of correlating the received signal with a known reference signal to extract the original binary data is feasible through spreading and de-spreading the spectrum. The concept of spread spectrum signaling is provided here to clarify the significance of the 10.23 MHz pseudo-random sequence. A block diagram showing the essential steps is given below.

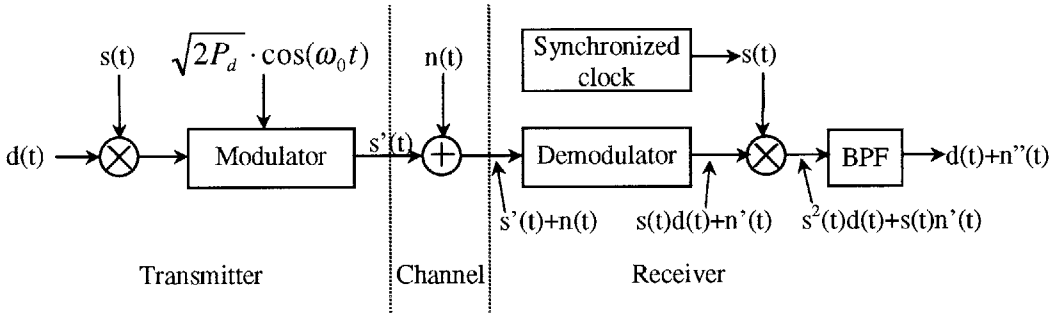

Figure 2.2: Spread Spectrum Block Diagram

On the transmitter side of the diagram, *d(t)* is the binary signal of ±1 with a clock rate of 50 Hz. It is given as the following:

$$d(t) = \sum_{n=-\infty}^{+\infty} D_n \cdot p(t - \tfrac{n}{f_d}) \Leftrightarrow S_d(f) = \frac{1}{f_d} \cdot \left(\frac{\sin \frac{\pi \cdot f}{f_d}}{\frac{\pi \cdot f}{f_d}} \right)^2 \qquad (2.1)$$

where D_n is the binary data sequence of ±1. $p(t)$ is a rectangular pulse of duration $\frac{1}{f_d}$

where f_d is the 50 Hz clock frequency of this signal $d(t)$. This 50 bps signal has a rather narrow sinc square spectrum S_d as shown below.

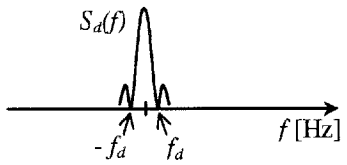

Figure 2.3: Spectrum of the Binary Data

$s(t)$ is the spread signal with a wider bandwidth whose significance is to "spread" the spectrum of $d(t)$. Its expression is similar to (2.1):

$$s(t) = \sum_{n=-\infty}^{+\infty} S_n \cdot p(t - \tfrac{n}{f_c}) \Leftrightarrow S_s(f) = \frac{1}{f_c} \cdot \left(\frac{\sin \frac{\pi \cdot f}{f_c}}{\frac{\pi \cdot f}{f_c}} \right)^2 \qquad (2.2)$$

Here, S_n is the binary *pseudo-random* sequence of ±1. The associated clock frequency is much higher at f_c of 10.23 MHz. Thus, its spectrum is still a sinc square but has a much broader bandwidth.

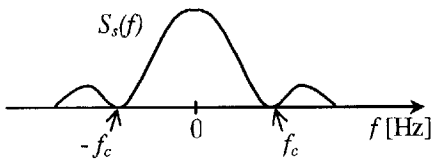

Figure 2.4: Spectrum of the 10.23 MHz Pseudo-random Signal

The resulting product of $d(t)s(t)$, if being multiplied synchronously, will have a power density spectrum that is similar to the spectrum of $s(t)$. The modulator then shifts the spectrum to a higher carrier frequency of 1575.42 MHz for the L_1 band or 1227.6

MHz for the L_2 band. In the diagram, P_d is the power of the carrier signal. Thermal noise and receiver noise of flat spectrum are being modeled as white-noise $n(t)$ and is added to the signal. At the receiver side, the demodulator will appropriately band-pass the signal and bring it back down to the base band. In time domain, the corresponding signal is back to $d(t)s(t)$ plus some band-limited white noise $n(t)$. An identical $s(t)$ is then synchronously multiplied with $d(t)s(t)+n(t)$. The result is $s^2(t)d(t)+s(t)n(t)$. Since $s(t)$ is a ± 1 signal, its square is simply 1. Also, $s(t)n(t)$ is still the same statistical noise $n(t)$. Consequently, the final output is $d(t)+n(t)$. The binary data signal $d(t)$ is retrieved along with some noise $n(t)$.

The timing in multiplying $s(t)$ with $d(t)s(t)+n(t)$ is very crucial. By sliding $s(t)$ back and forth and integrating over one period of $d(t)$, the correlation peak will occur when $s(t)$ is perfectly aligned with the $s(t)$ component in $d(t)s(t)+n(t)$. In a GPS receiver, there are typically four or more channels available to retrieve the data from four GPS satellites. The four correlation operations will provide the relative peak times or relative delays among the channels. Essentially, correlating the received signals with their corresponding spread signal $s(t)$ is the key in precision differential delay measurements.

To show how much noise power being reduced in the final discrete sequence of data, let's suppose that the signal $d(t)s(t)+n(t)$ is sampled at the Nyquist rate of $2 \cdot 10.23\text{MHz} = 20.46$ MHz. The correlation will be done in discrete method as shown below.

Let $y[n]$ be the sampled sequence of $d(t)s(t)+n(t)$ and $s[n]$ be the samples of $s(t)$. Also, assume that the integration duration is one period of $d(t)$ which is 1/50 second. This corresponds to summing N samples where N is (1/50) second x 20.46 million

samples / second ≈ 0.4 million samples. The retrieved data sequence D'_n is then defined as follows:

$$D'_n = \frac{1}{N} \cdot \sum_{m=n \cdot N}^{(n+1)N} y[m] \cdot s[m]$$

$$= \frac{1}{N} \cdot \sum_{m=n \cdot N}^{(n+1)N} \left(s[m]d[m] + n[m] \right) \cdot s[m]$$

$$= D_n + \frac{1}{N} \cdot \sum_{m=n \cdot N}^{(n+1)N} \left(n[m] \right) \tag{2.3}$$

From (2.3), the expectation of the retrieved sequence D'_n is seen to be the same as the original data sequence D_n. The variance of each sample is the original noise power scaled down by N. This is because the average of N identically distributed uncorrelated random variables has a variance that is $1/N$ of the variance of one of the random variables. In this case, although the signal $d(t)s(t)$ is about 30 dBW below thermal noise level, the sequence D_n can certainly be recovered with noise being reduced by $10 \cdot \log(0.4e6) = 56$ dB. Thus, there is still a 26 dB signal to noise ratio.

2.4 Jamming Signal Characteristics

The trouble begins when there is one or more additional signal sources in the environment that emulate the GPS signal characteristics with an intent to jam the GPS signal. These so-called jammers are designed to have the same carrier frequency and bandwidth as that of the GPS. In addition, the power of those jammers is naturally expected to be much larger, at least by many orders of magnitude. Consequently, regular GPS receiver systems will fail to operate in such a hostile environment.

If the GPS signal were to be recovered in the presence of jammers, it would certainly require additional signal processing. Techniques of adaptive antenna array

processing are the keys to solving the proposed problem. Various types of general adaptive array processing algorithms can be found in the literature. Each approach is usually intended for a specific jamming problem, often involving trade-off between different measures of performance. As more parameters are added to the model of the problem, many general existing algorithms will no longer work effectively. New clever techniques will need to be developed and tested to deal with those special circumstances. In this project, the problem is concerned with not only nulling one or several direct-path wide-band jammers but also their reflected multi-path replicas from the aircraft body. The multi-path characteristics cannot be easily estimated because we are not certain about what fraction of the jamming signals are reflected and from which parts of the plane. Thus, in order to accurately evaluate the performance of the space-time adaptive array algorithms in the presence of multi-path, it is necessary to carry out a real experiment to study the multi-path effects. These will essentially be determined by the space-time covariance matrices being formed out of the real data as will be described in a later section. Based on the covariance matrices, data will be generated to simulate signals received in a jamming environment with multi-path effects. Then, an adaptive array algorithm that exploits both temporal and spatial degrees of freedom will be implemented and tested on the simulated data. A thorough analysis will be done to study the problem and possible solutions.

3 Data Collection

This section describes the essential aspects of the experiment that has been conducted to acquire the data for this study of the multi-path problem. The carrier frequencies being transmitted are actual GPS frequencies at 1575.42 MHz (L_1) and 1227.6 MHz (L_2). The modulating signals are pseudo random sequences of 10 Mhz broad-band spectrum. Thus, the transmitting signals have the exact frequencies and spectrum as the actual GPS signals. In addition, these supposedly jamming signals have a much higher power, namely about 40 to 50 dB above the thermal noise power. However, the duration of the transmission is relatively short, lasting about 1 ms for each data set, such that the transmitted signal would not actually jam out those real GPS systems in the area during the data collection.

The transmitter is located about a mile away from the receiver. At the receiver end, the main set up can be described as follows: a seven-element antenna is placed on top of an F-16 fighter plane. A similar setup is done for the F-15 plane. The receiver and other equipment are secured inside the plane. The plane is mounted on a revolving pedestal on top of a tower. The plane can be tilted up or down at different elevation or depression angles. At any elevation, it can also be rotated around 360 degrees. Thus, it is possible to position the plane such that the jamming signal is effectively coming from any desired direction with respect to the plane. This allows investigation of the multi-path effects for various directions of arrival of the jamming signals. Data for the following depression angles have been collected: 0, 5, 10, 15, 20, 22, 24, 26, 28, and 30 degrees for each carrier frequency. At each depression angle, the plane is rotated 360

degrees where data is collected at every quarter of a degree. The transmitter alternates the signal between right-hand circular polarization and left-hand circular polarization.

Due to the channel mismatch in the entire receiver system, the gain and phase are different from one channel to another. Moreover, the analog low-pass filters for the channels are not identical. These imperfections result in the necessity for obtaining calibration signals and performing channel equalization when processing the data. The next section will show how to generate the equalization filters based on the calibration data so that the effect of channel mismatch can be eliminated from the actual signals. The procedure for taking the calibration data is as follows: every few degrees in azimuth, the switches are toggled such that all channels receive the same calibration signal from a single horn mounted at a fixed location in the open space near the pedestal. If the receiver system was ideal, then the data from different channels would be identical. Since the data are not identical, their variations from channel to channel allow the construction of equalization filters which can be applied to the actual data received from the antenna.

The signal path and the calibration path are illustrated in the following figure:

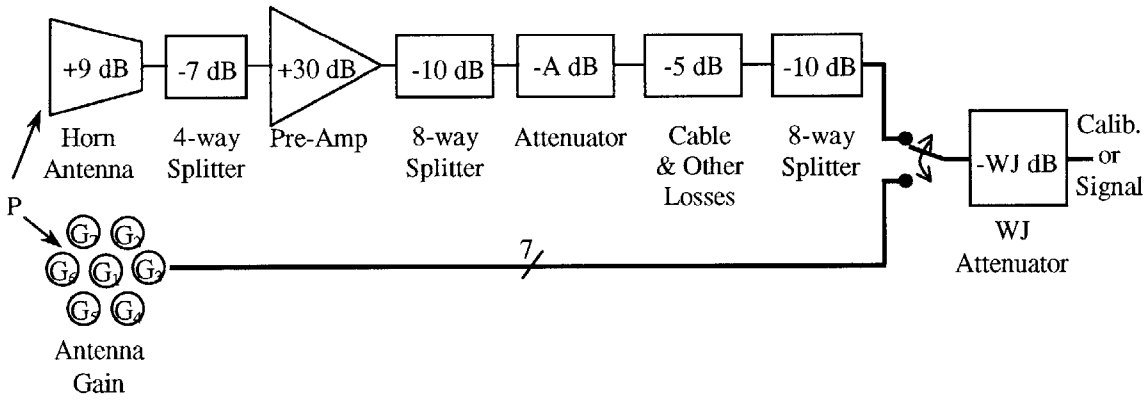

Figure 3.1: Attenuation Paths

Note that the attenuation settings denoted by A and WJ are different for each depression angle cut. These settings were selected to maximize the signal-to-noise ratio since the effective antenna gain is smaller at a deeper depression. Consequently, plotting the signal power for each depression angle reveals the antenna pattern for that cut, however, getting the absolute power level would require some computation based on the attenuation settings.

The signals are low-passed to 10 MHz before being sampled at 25.6 MHz. The data collected at each azimuth/depression angle pair consists of 8 by 4096 samples of twos-complement 12 bit integers, which are later converted to 16 bit integers. Since there are only 7 antenna elements, the row of data which corresponds to the terminated channel is removed. The remaining rows of data are sorted in the order of the antenna element numbers.

4 Inphase-Quadrature Conversion

The receiver band-passes the spectrum at the L_1 or L_2 radio frequency to a 10 MHz band-width. The spectrum is then shifted down to an intermediate frequency of 6.4 MHz before being sampled at 25.6 MHz. Since the discrete real data are still at the intermediate frequency, it is necessary to convert the data down to the base-band in the form of inphase and quadrature components. Equalization and space-time signal processing are later performed on the inphase-quadrature data rather than directly on the original real data. The following figure illustrates the steps in the IQ conversion.

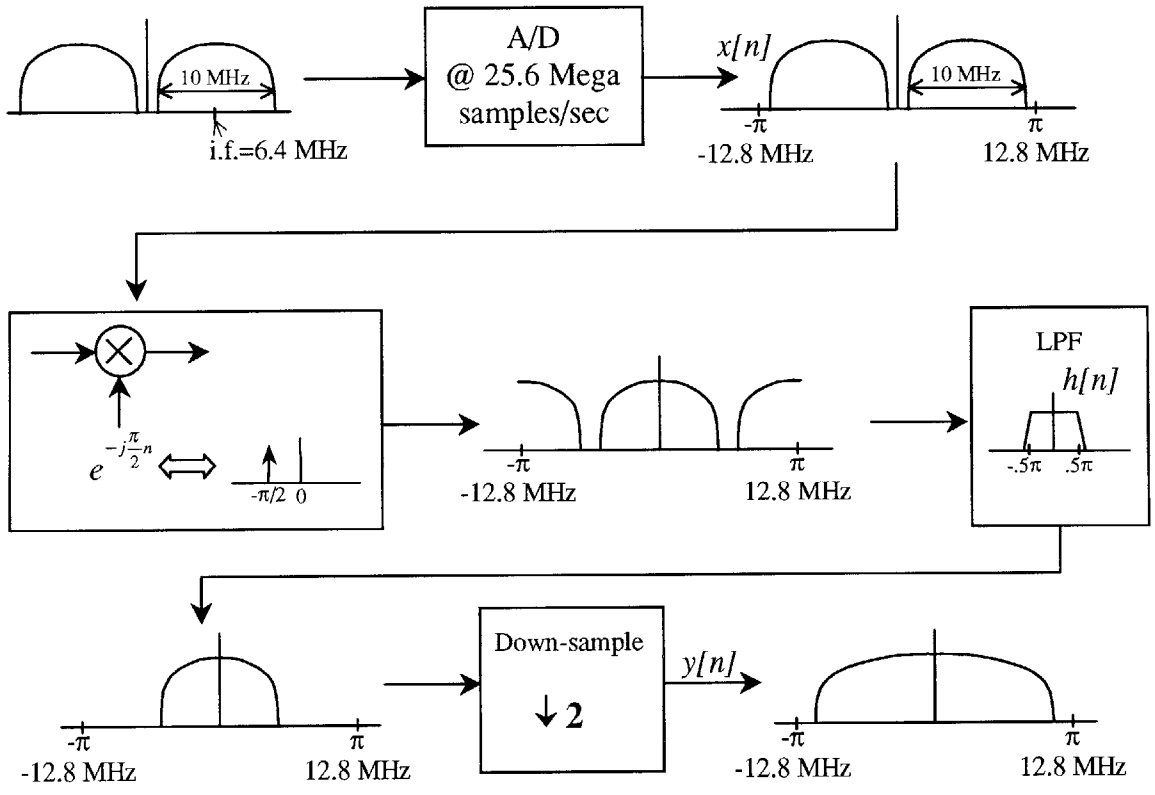

Figure 4.1: Inphase Quadrature Conversion

The received data are real, thus its spectrum is perfectly symmetric around 0. It also looks symmetric around 0.5π – the i.f. frequency. The data are first multiplied by a sequence of *1*, *-j*, *-1*, *j*, etc. Equivalently, the spectrum is shifted left by $\pi/2$. A low-pass filter with a cut-off frequency of $\pi/2$ is applied so that only one side of the original spectrum remains, centered at zero frequency. Although the shape looks symmetric, the spectrum may no longer be perfectly symmetric and thus, the data become complex. The complex data can also be down-sampled by 2 to maintain its original data rate without any aliasing.

By taking advantage of low-passing followed by down-sampling, reduction in computation can be significantly achieved through polyphase implementation. In a direct implementation following the block diagram as shown above, low-passing would require M *complex* multiplication's with the complex data, where M is the length of the low-pass, to generate one sample after the low-passing stage. Equivalently, it takes 2M *real* multiplication's since the data is a complex sequence after being multiplied with $e^{j(\pi/2)n}$ while the low-pass is real. Then, in the down-sampling stage, every other sample is thrown away. This means for each final output sample, it requires a total of 4M real multiplication's plus the associated number of additions.

A more clever scheme that combines all three stages can reduce the number of real multiplication's to M per final output sample. First, consider splitting the data stream into its real and imaginary sequences and combine them later. This is possible since the low-pass is real.

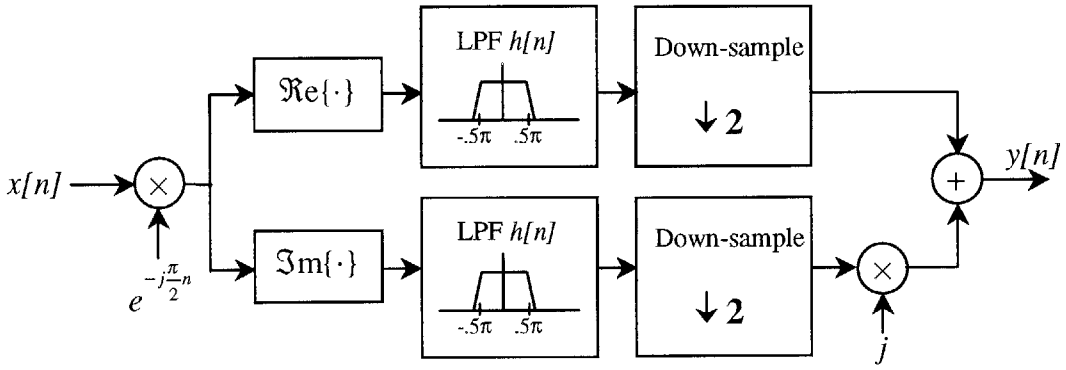

Figure 4.2: Real/Imaginary Data Stream in IQ Conversion

Note that the real part of $x[n] \cdot e^{-j(\pi/2)n}$ is simply *{x[0],0,-x[2],0,x[4],0,-x[6],0 . . .}* and the imaginary part is simply *{0,-x[1],0,x[3],0,-x[5],0,x[7] . . .}*. In both data streams, every other sample is *0*, which will be useful when data streams are split further into 2 sequences of even and odd indices.

Polyphase implementation of the low-passing and down-sampling stages can be illustrated in the following figure:

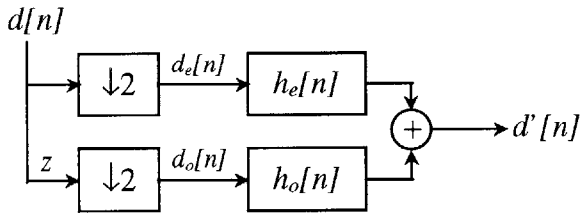

Figure 4.3: Polyphase Implementation of Low-passing and Down-sampling

Instead of passing *d[n]* through a low-pass filter *h[n]* and then throwing away every other sample, *d[n]* can be split into 2 sequences: one consisting of the even-index samples of *d[n]* and the other consisting of the odd-index samples of *d[n]*. The even

sequence is convolved with the similarly-defined even-index samples of $h[n]$. The odd sequence $d_o[n]$ is convolved with the odd sequence $h_o[n]$. Combining the two by addition results in the equivalent output.

Now, applying the polyphase implementation back in Figure 4.3 and recognizing that the odd sequence of the real part of $x[n] \cdot e^{-j(\pi/2)n}$ and the even sequence of the imaginary part of $x[n] \cdot e^{-j(\pi/2)n}$ are both zero sequences, a simplified IQ implementation is derived.

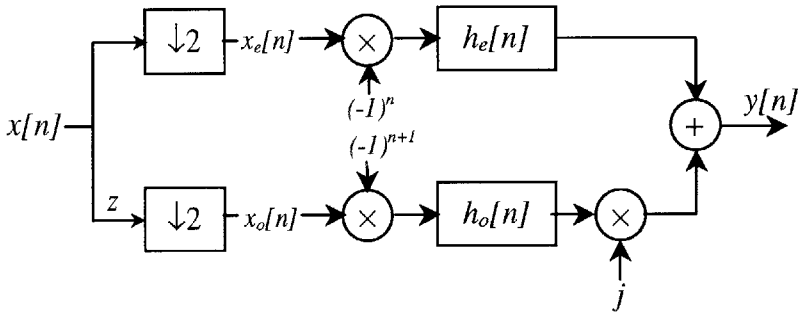

Figure 4.4: A Simplified IQ Implementation

Note that for each output sample of $y[n]$, it requires only a total of M multiplication's with the odd and even samples of the low-pass filter since $h_e[n]$ and $h_o[n]$ each has a length of M/2 samples.

The next page shows two typical plots of the actual data spectrum before and after being converted to the inphase-quadrature format.

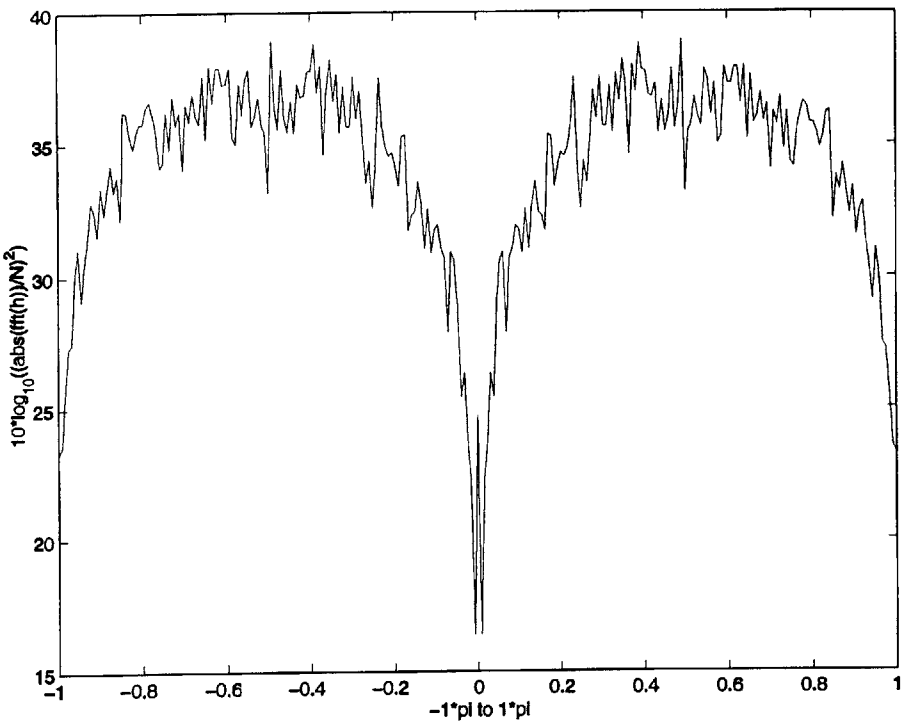

Figure 4.5: A Typical Power Density Spectrum of the Real Data

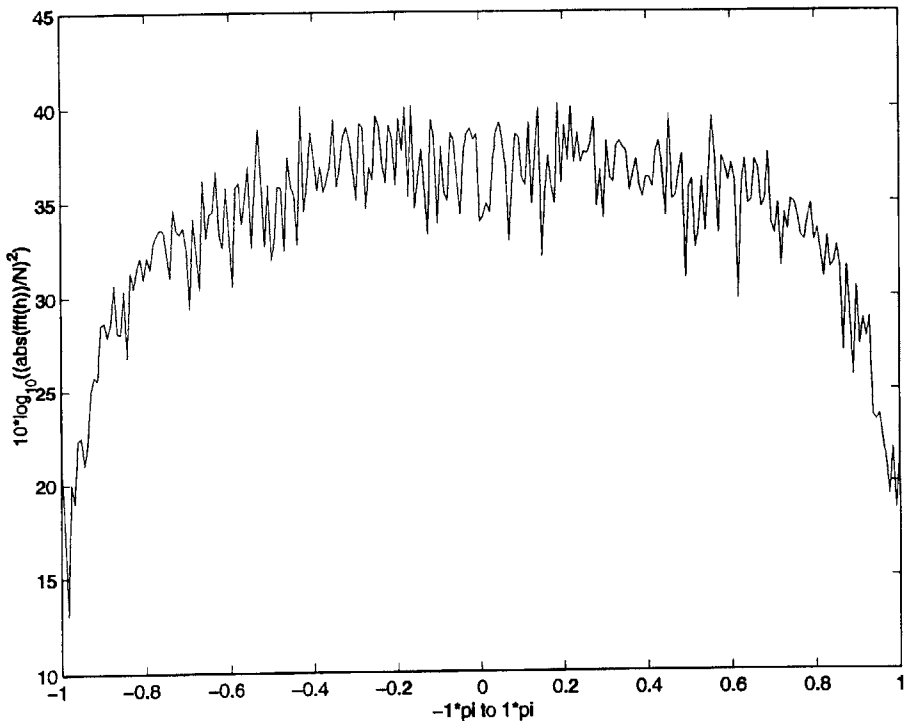

Figure 4.6: A Typical Power Density Spectrum of the Complex Data

5 Channel Equalization

An important characteristic of adaptive array processing is the capability of making use of the phase differences among the received signals from various antenna elements. Ideally, any differences in phase or amplitude between two received signals from two antenna elements are expected to attribute to the antenna array arrangement as well as the arrival direction of the signal. However, in an actual receiver system, the channels are not perfectly identical, thus additional mismatch in the received signals is introduced. Such misalignment due to an imperfect receiver must be compensated so that the differences in the received signals can truly be exploited as a result of the antenna arrangement.

In the following sections, the system channel mismatch is carefully modeled. A method for digitally equalizing the channels is also given. Next, the equalization method is tested on simulated data and the results are presented. The last section in this chapter discusses the performance of equalization on the actual data and its implications to space-time adaptive processing.

5.1 Modeling Channel Mismatch

In a GPS multi-channel receiver, each channel has an analog low-pass filter for limiting the bandwidth of the signals to 10 MHz before the conversion to digital data. Since the low-pass filters are analog circuits, there exist variations from one low-pass to another. In addition, the gain and phase are different from one channel to another. The objective is to account for those variations by introducing the discrete equalizer as shown below.

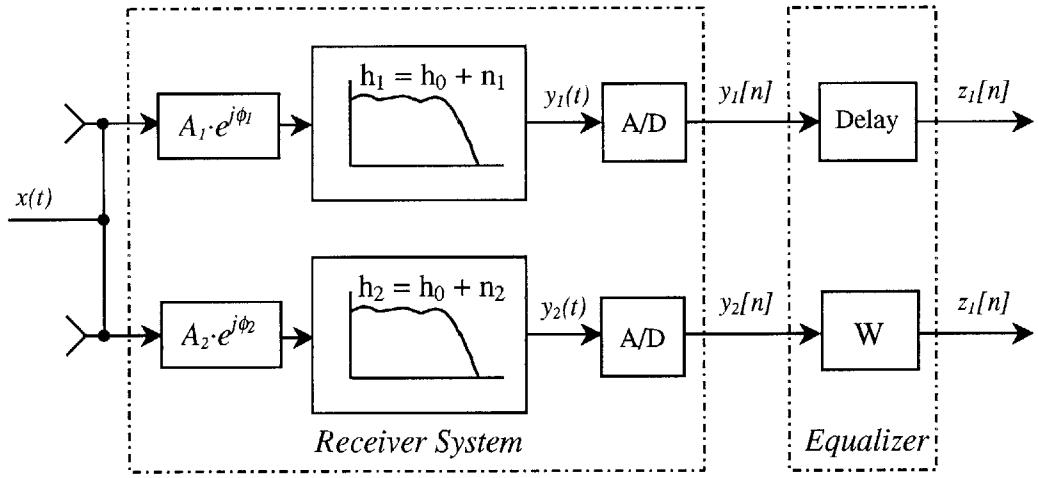

Figure 5.1: Channel Mismatch and The Discrete Equalizer

The block diagram in Figure 5.1 shows that each channel has its own gain and phase. These parameters are fairly constant and can all be accounted for in the equalizer. The two low-pass filters are each made up of an identical low-pass h_0 plus some unknown variation n_i which is different for each channel. As a result, $y_1(t)$ is different from $y_2(t)$ and so are $y_1[n]$ and $y_2[n]$, besides the fact that they have different gain and phase. The purpose of the equalizer is to calibrate the two channels so that the two output signal $z_1[n]$ and $z_2[n]$ will have less discrepancy than the two equalizer inputs. These two signal $z_1[n]$ and $z_2[n]$ should be as similar as possible since the inputs to the system are tied to the same calibration signal $x(t)$.

5.2 Computing Equalization Filter

The criteria for generating the equalizer is based on minimizing the mean-square-error of the output signals.

Let the length of the filter W be $(2d+1)$ and the length of the two sample sequences $y_1[n]$ and $y_2[n]$ be N. The MSE solution for W is found to be of the following:

$$\boldsymbol{W} = \left(\boldsymbol{R}_{y_2y_2}^{-1} \cdot \boldsymbol{r}_{y_2y_1}\right)^{\mathrm{H}} \tag{5.1}$$

where the *(2d+1)×(2d+1)* Hermitian matrix $\boldsymbol{R}_{y_2y_2}$ is defined as:

$$\boldsymbol{R}_{y_2y_2} = \begin{bmatrix} E\{y_2[n]\cdot y_2^*[n]\} & E\{y_2[n]\cdot y_2^*[n-1]\} & \cdots & E\{y_2[n]\cdot y_2^*[n-2d]\} \\ E\{y_2[n-1]\cdot y_2^*[n]\} & E\{y_2[n-1]\cdot y_2^*[n-1]\} & \cdots & E\{y_2[n-1]\cdot y_2^*[n-2d]\} \\ \vdots & \vdots & \ddots & \vdots \\ E\{y_2[n-2d]\cdot y_2^*[n]\} & E\{y_2[n-2d]\cdot y_2^*[n-1]\} & \cdots & E\{y_2[n-2d]\cdot y_2^*[n-2d]\} \end{bmatrix} \tag{5.2}$$

with *E* denoting the expected value of the enclosed quantity. The *(2d+1)×1* vector $\boldsymbol{r}_{y_2y_1}$ is likewise defined as:

$$\boldsymbol{r}_{y_2y_1} = E\left[\begin{pmatrix} y_2[n] \\ y_2[n-1] \\ \vdots \\ y_2[n-2d] \end{pmatrix} \cdot \left(y_1^*[n-d]\right)\right] = \begin{bmatrix} E\{y_2[n]\cdot y_1^*[n-d]\} \\ E\{y_2[n]\cdot y_1^*[n-(d-1)]\} \\ \vdots \\ E\{y_2[n]\cdot y_1^*[n+d]\} \end{bmatrix} \tag{5.3}$$

In computing the estimated $\boldsymbol{R}_{y_2y_2}$ and $\boldsymbol{r}_{y_2y_1}$, the data sequence is assumed to be ergodic so that the expectation of a quantity is simply its time average. For example,

$$E\{y_2[n]\cdot y_1^*[n-m]\} = \frac{1}{N}\cdot\sum_{n=1}^{N} y_2[n]\cdot y_1^*[n-m] \tag{5.4}$$

As shown in the diagram, $y_1[n]$ is simply delayed by *d* samples since W is a d-sample delayed non-causal FIR filter. Once the equalizer has been computed, the system can be used to receive an actual incoming signal, which is different at each antenna element. The previously computed equalizer can then be applied to the receiver's output signals to compensate for the channel mismatch.

The same equalizer can be used for another signal received at a later time only if the variations among the channels remain within an acceptable threshold. In practice, those errors in the receiver drift over time especially as the system's temperature changes.

Thus, the system is set in calibration mode frequently to acquire the calibration data so that the equalizer can be updated.

5.3 Evaluating Equalization Method

The first test is concerned with determining the necessary number of taps for the equalization filter in order to achieve a near optimal performance for a given number of taps in the low-pass filter. The simulation set-up is shown in the Figure 5.2. The input signal is a zero-mean Gaussian random sequence. It is band-limited before being fed to two low-pass filters, both of which are made up of the same low-pass but are perturbed by different error sources. The scale factor can be set to simulate the severity of the mismatch in the low-passes. Then, there is the option of equalizing the original real signals or converting the data to IQ prior to equalization. The differences between the two options will be discussed later. The two signals x_1 and x_2 are equalized for a range of taps. The equalization performance is evaluated by computing the residual power before and after the equalization process. The residual power indicates the normalized error power between two signals s_1 and s_2 and is defined as follows:

$$RP_{s1,s2} = 10 \cdot \log_{10}\left(\frac{E\{(s_1 - s_2)^2\}}{E\{(s_1)^2\}}\right) = 10 \cdot \log_{10}\left(\frac{\frac{1}{N}\cdot\sum_{1}^{N}(s_1 - s_2)^2}{\frac{1}{N}\cdot\sum_{1}^{N}(s_1)^2}\right) \quad [dB] \qquad (5.5)$$

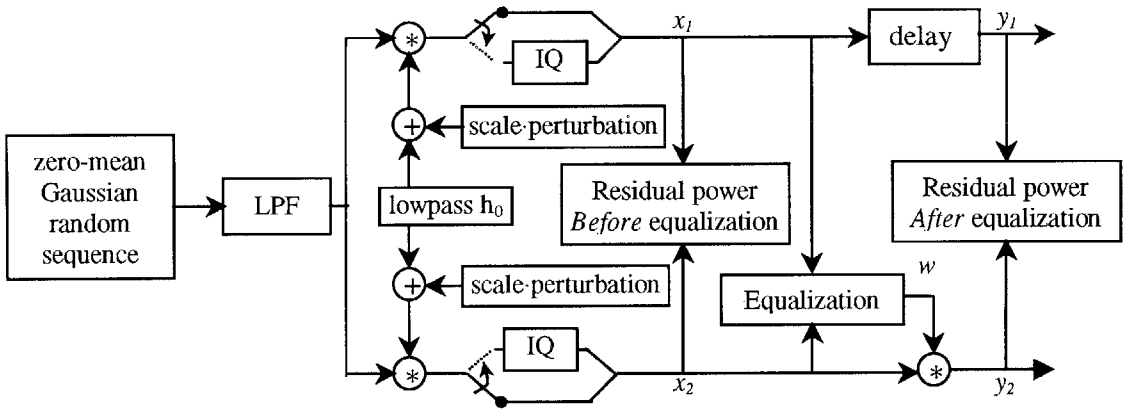

Figure 5.2: Residual Power Before and After Equalization

Several parameters can be set for various cases. First is the scaling factor for the low-pass noise. This parameter affects the absolute residual power of the signals before and after the equalization process. It however does not affect the relative improvement at a particular number of taps for the low-pass and for the equalizer. Thus, in all examples shown on the following pages, the scale is picked at 0.01. This number sets the residual power of the signals before equalization to be about -20 dB. In the first two plots, the real signals are considered. When the low-pass has 31 taps, the residual power of the output signals does not improve much until the number of taps for the equalizer gets beyond 31 taps. Similarly as in the second plot, when 51 taps are used for the low-pass, more than 51 taps are required to observe a significant improvement. The same parameters are used in the next two simulations, except that the signals are converted to inphase-quadrature form before being equalized with a complex equalizer. By using complex taps on the complex signals, an equivalent performance can be achieved with only half the number of taps used in the case of real signals. In all cases, once the number of equalization taps exceeds the "fall-off" point, only a very slow rate of

improvement can be achieved for any additional taps. Thus, in equalizing the actual data, this optimal number of equalization taps is determined to optimize the computation. As mentioned earlier, the actual data are all converted to inphase-quadrature form for equalization and processing. The advantage is most obvious when only a few taps is used. Considering the case in which only one complex equalization tap is allowed: one complex equalization tap is sufficient to adjust the gain and phase of the signal. In the case of real signals, two real taps may not accomplish the same task with a similar resulting residual power.

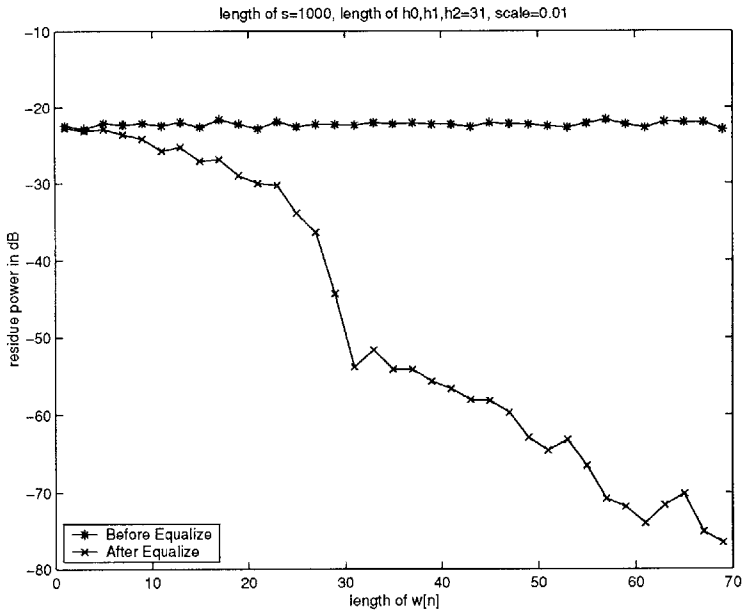

Figure 5.3: Example 1 of Residual Power as a Function of Filter Length

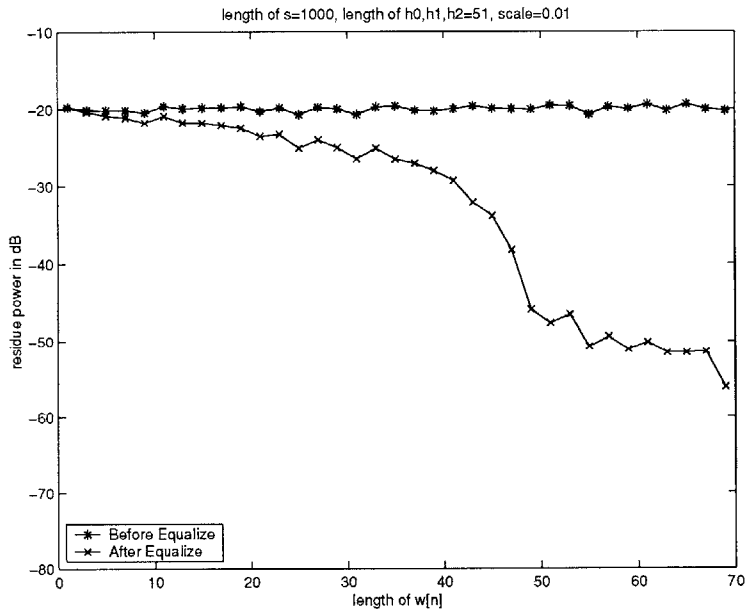

Figure 5.4: Example 2 of Residual Power as a Function of Filter Length

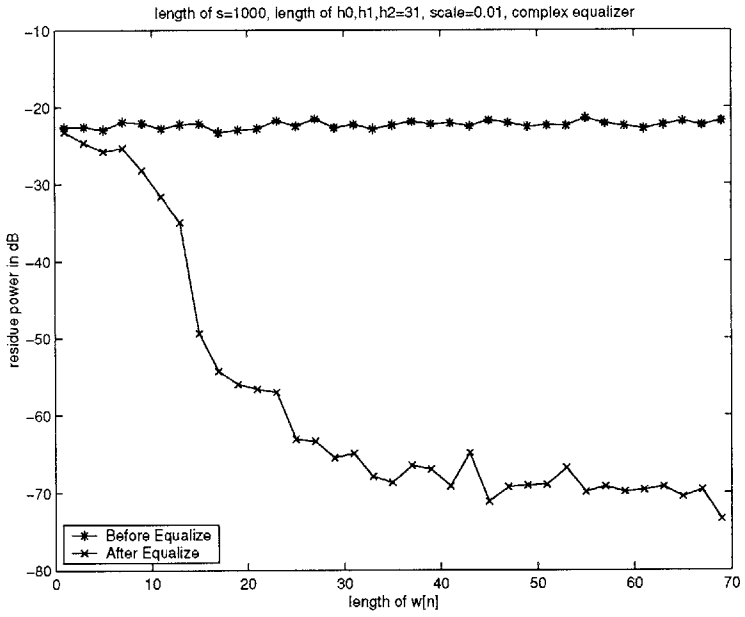

Figure 5.5: Example 3 of Residual Power as a Function of Filter Length

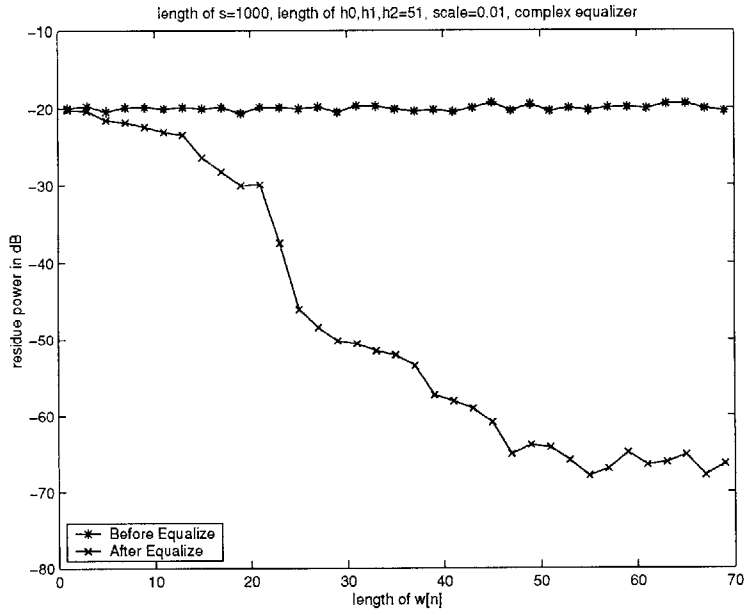

Figure 5.6: Example 4 of Residual Power as a Function of Filter Length

Picking the optimal number of taps for the equalization filter is important in achieving a result near the theoretical limit but without sacrificing unnecessary computation. Thus, the optimal length for the equalization filter is always used for all cases in this next simulation. The simulation is now concerned with how signal-to-noise ratios might limit the final residual power for several practical scenarios.

The following three figures describe the set-up for evaluating the equalization performance as various SNR's are considered.

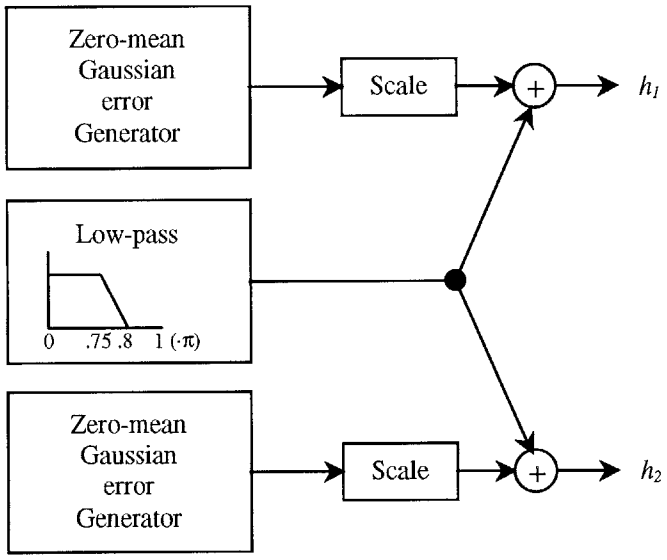

Figure 5.7: Simulation of Low-pass Filters with Varied Pass-band Ripples

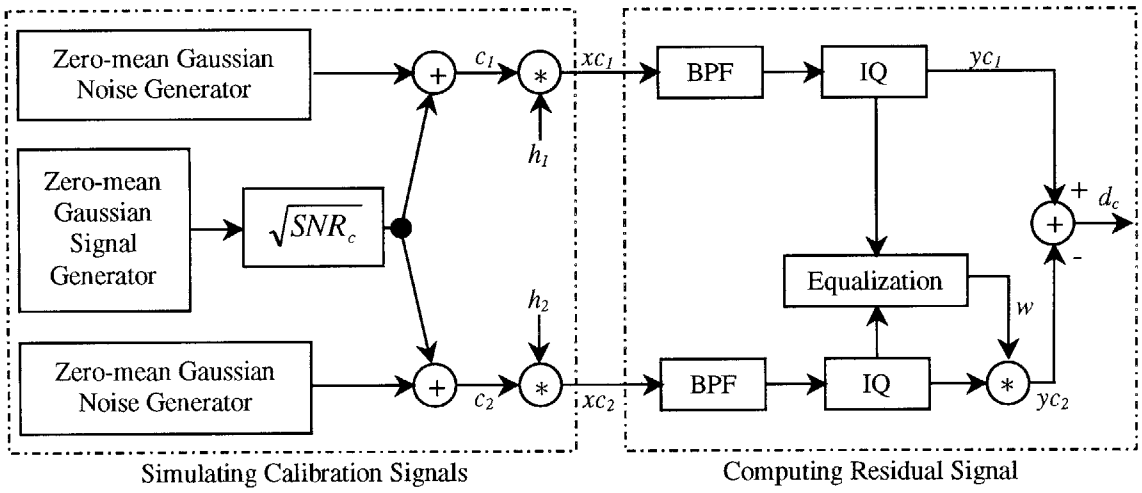

Figure 5.8: Simulation of Calibration Signals and Residual Signal

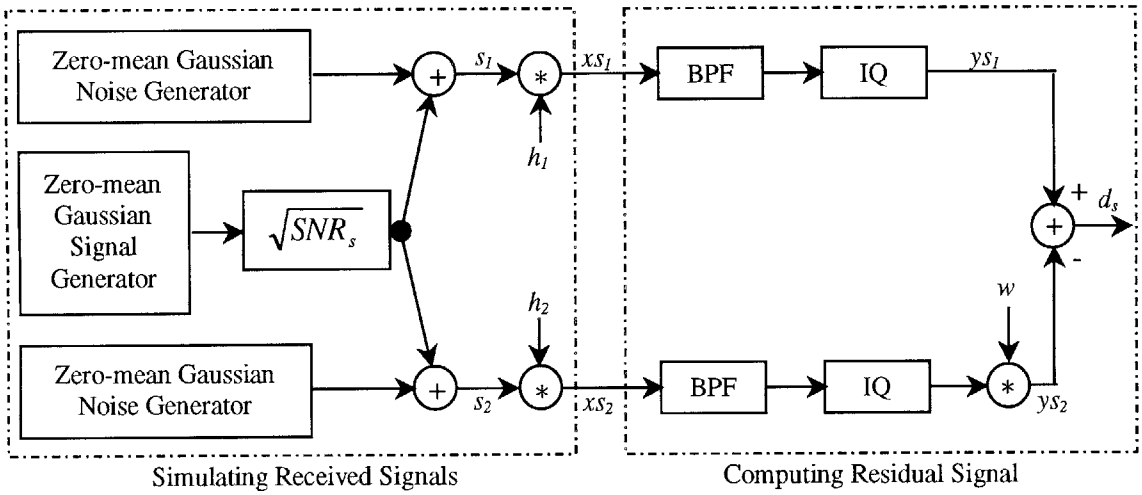

Figure 5.9: Simulation of Received Signals and Residual Signal

In Figure 5.7, the two low-pass filters h_1 and h_2 are generated by adding independent zero-mean Gaussian error to one common low-pass. The scale factor determines how different the two low-pass filters are. To measure the degree of mismatch, h_2 is equalized to h_1 and the residual power is computed for these post-equalized low-pass filters.

In Figure 5.8, c_1 and c_2 are the two calibration signals of signal-to-noise ratio SNR_c. These two signals are low-passed by h_1 and h_2, and thus the two received calibration signals xc_1 and xc_2 have a degraded quality due to the unequal h_1 and h_2. The second block in the same figure uses an equalization filter w such that after the equalization, the two channels will have a minimal residual power. As shown in the figure, the two received signals are first band-pass filtered and then converted to inphase-quadrature form. The equalization block processes these two complex signals and produces a filter w for equalizing the second channel to the first channel data. The difference of the signals d_c can then be computed as a measurement for how well the two channels can be equalized.

Figure 5.9 shows the simulation of the "actual" signals which have a different signal-to-noise ratio but are low-passed by the same h_1 and h_2. The two received signals are band-passed and converted to IQ as in the calibration case. The two complex signals are then equalized using the equalization filter generated earlier. This is what being done in the actual experiment: the signals at different elements of the antenna array are not supposed to be identical and thus, only the equalization filter generated from the calibration signals are used to undo the effects caused by the unequal low-passes. Here, because the simulated signals s_1 and s_2 come from one single source, the residual power of the signals after being processed and equalized is an indication of how well the equalization filter performs on the "actual" signals.

By setting the scale factor in the first figure and signal-to-noise ratios for the two types of simulated signals, various cases can be simulated and observed.

	Case 1	Case 2	Case 3	Case 4	Case 5
Low-pass noise scale	0.0001	0.01	0.01	0.01	0.01
SNR of calibration signals	50 dB	50 dB	40 dB	80 dB	45 dB
SNR of actual signals	60 dB	60 dB	60 dB	60 dB	50 dB
Residual power of the equalized low-passes	-70 dB	-35 dB	-35 dB	-35 dB	-35 dB
Residual power of calibration signals before equalization	-47 dB	-24 dB	-21 dB	-23 dB	-22 dB
Residual power of calibration signals after equalization	-47 dB	-47 dB	-37 dB	-74 dB	-42 dB
Residual power of actual signals before equalization	-57 dB	-24 dB	-24 dB	-24 dB	-23 dB
Residual power of actual signals after equalization	-57 dB	-47 dB	-44 dB	-49 dB	-45 dB

Table 5.1: Equalization Performance for Different SNR's

Case 1 is trivial: if the variation between the two low-passes is small such that the filters can practically be considered identical, then equalization is not necessary. The residual power before equalization is already optimal and is the same as after equalization. The next few cases are more interesting and practical where the mismatch in the low-pass does cause a problem. Case 2 shows that the calibration signals have a SNR of 50 dB. Before equalization, the signals have a residual power of only -24 dB, but after equalization, the residual power is down to -47 dB, which is 3 dB from its theoretical limit. When the equalization filter generated from the calibration signals is used to equalize the actual signals of 60 dB SNR, a similar improvement can be seen but the residual power is *not* down to -57 dB. Thus, the residual power is limited not only by the SNR of the signals to be equalized but also by the SNR of the calibration signals. However, the limitation is not strictly the negative SNR of the calibration signals. As

shown in Case 3 where there is a bigger difference in the SNR's, the actual signals can be equalized down to -44 dB, although the calibration signals have only 40 dB of SNR. It can be proven that the limit is really 2 times the negative SNR of the calibration signals, but in practice, the result is far from this limit. Case 4 is about how much the residual power can be improved if the SNR of the calibration signals is much greater than that of the signals. Certainly, the residual power gets better, but not a lot better. The equalizer computed from the calibration signals of a finite SNR is never a perfect equalizer. Thus, the residual power of the signals in Case 4 after being equalized is only as low as -49 dB and not -57 dB. The first four cases illustrate how the performance is affected by varying certain parameters. In Case 5, more practical SNR's are used and the results are just what is expected based on the given SNR's.

5.4 Equalization Performance on the Collected Data

In this section, the general results of equalization on the F-16 data are presented. The table below shows the residual power in dB of a typical calibration data set after being equalized with 31 complex taps. Note that each of the 7 rows corresponds to each of the 7 possible channels to be used as the reference channel.

	Ch. 1	Ch. 2	Ch. 3	Ch. 4	Ch. 5	Ch. 6	Ch. 7
Reference Ch. 1	-∞	-33	-35	-34	-34	-33	-33
Reference Ch. 2	-33	-∞	-35	-36	-39	-38	-43
Reference Ch. 3	-35	-35	-∞	-39	-39	-35	-35
Reference Ch. 4	-34	-36	-39	-∞	-37	-37	-37
Reference Ch. 5	-33	-39	-35	-36	-∞	-36	-39
Reference Ch. 6	-33	-39	-35	-37	-36	-∞	-39
Reference Ch. 7	-33	-43	-35	-36	-40	-38	-∞

Table 5.2: Typical Residual Power of Collected Data

If only one complex tap is used in the equalizer for adjusting the gain and phase of the calibration signals, the resulting residual power would correspond to the residual power of the signals before compensating for any mismatch in the low-pass filters. The next table shows a typical result for a 1-tap equalizer.

	Ch. 1	Ch. 2	Ch. 3	Ch. 4	Ch. 5	Ch. 6	Ch. 7
Reference Ch. 1	-∞	-29	-26	-24	-22	-30	-27
Reference Ch. 2	-29	-∞	-25	-25	-19	-28	-24
Reference Ch. 3	-26	-25	-∞	-32	-20	-25	-23
Reference Ch. 4	-24	-25	-32	-∞	-18	-23	-22
Reference Ch. 5	-22	-20	-20	-18	-∞	-22	-26
Reference Ch. 6	-30	-28	-25	-23	-22	-∞	-28
Reference Ch. 7	-27	-24	-23	-22	-27	-28	-∞

Table 5.3: Typical Residual Power of Collected Data with Single Tap in Equalizer

Subtracting one table from the other results in a measure of how much the equalization has compensated for the channel mismatch. The typical values are in the range of -10 to -20 dB of improvement. By repeating the computations with different numbers of taps, it is found that the residual power approaches the optimal values when the number of taps in the equalizer is about 15 to 20 taps. In Table 5.2, the near-optimal residual power implies that the calibration signals have a SNR of about 40 dB. This SNR is less than desired for the space-time signal processing, but that is the best one could achieve given real-world limitations on the GPS transmission power.

6 Multi-path Characterization

After the data have been converted to inphase-quadrature and equalized, space-time covariance matrices are formed for each elevation and azimuth angle. Essentially, these matrices are sufficient to characterize the effects of multi-path if one assumes that the signals are zero-mean Gaussian samples whose auto-correlation or cross-correlation functions have a finite duration. The relative magnitudes of the eigenvalues for each covariance matrix indicate how uncorrelated the signals have become due to the multi-path scattering. Thus, plotting their eigenvalues reveals the severity of the multi-path phenomenon for any arrival angle of the jamming signal. This chapter elaborates on forming the covariance matrices and their implications to multi-path. The next chapter will provide a discussion on how simulated data can be generated based on these covariance matrices for a single jamming signal as well as multiple jamming sources.

6.1 Space-Time Covariance Matrices

For each data set which corresponds to one direction of arrival of the jamming signal, a space-only correlation matrix of the antenna elements can be computed as follows:

$$\hat{\boldsymbol{R}}_{\bar{\theta},1} = \frac{1}{Q} \cdot \sum_{n=1}^{Q} \vec{z}_{\bar{\theta},1}[n] \cdot \vec{z}_{\bar{\theta},1}^{H}[n] \tag{6.1}$$

where $\vec{z}_{\bar{\theta}}[n]$ is a 7×1 column vector representing the 7-channel received signal at time n in the inphase-quadrature equivalence.

To get the *space-time* correlation matrix for L taps, the similar definition is used:

$$\hat{\boldsymbol{R}}_{\vec{\theta},L} = \frac{1}{Q} \cdot \sum_{n=1}^{Q} \vec{z}_{\vec{\theta},L}[n] \cdot \vec{z}_{\vec{\theta},L}^{H}[n] \tag{6.2}$$

where $\vec{z}_{\vec{\theta},L}[n]$ is arranged from the original data sequence $\vec{z}_{\vec{\theta},1}[n]$ as given below:

$$\vec{z}_{\vec{\theta},L}[n] \equiv \begin{bmatrix} \vec{z}_{\vec{\theta},1}[n] \\ \vec{z}_{\vec{\theta},1}[n-1] \\ \vdots \\ \vec{z}_{\vec{\theta},1}[n-L+1] \end{bmatrix} \tag{6.3}$$

6.2 Eigenvalues and Eigenvectors of Covariance Matrices

Since all the matrices are Hermitian, they can equivalently be expressed in terms of their eigenvalues e_i's and eigenvectors v_i's as shown.

$$\hat{\boldsymbol{R}}_{\vec{\theta},L} = \sum_{i=1}^{7 \cdot L} e_i \cdot \vec{\boldsymbol{v}}_i \cdot \vec{\boldsymbol{v}}_i^{H} \tag{6.4}$$

Consider the spatial-only covariance matrix: if the signals are completely correlated with one another, the matrix will have a rank of one. Consequently, there will be one large eigenvalue equivalent to the signal power. The remaining eigenvalues will be small with magnitudes equivalent to the noise power. In a multi-path environment, the received signals are likely to be de-correlated due to the multi-path scatterers. Correspondingly, some of the small eigenvalues will increase in magnitude. The more uncorrelated the signals become, the bigger these eigenvalues get. At the other extreme, where the signals are completely uncorrelated, the matrix will have full rank and the eigenvalues will all have comparable magnitudes.

For each space-time covariance matrix where $L>1$, the matrix can be partitioned into $L\times L$ blocks with each block being a 7×7 correlation matrix. The general form is as follows:

$$\hat{\boldsymbol{R}}_{\vec{\theta},L}=\begin{bmatrix} \hat{\boldsymbol{R}}_{\vec{\theta},1}^{(0)} & \hat{\boldsymbol{R}}_{\vec{\theta},1}^{(1)} & \hat{\boldsymbol{R}}_{\vec{\theta},1}^{(2)} & \cdots & \hat{\boldsymbol{R}}_{\vec{\theta},1}^{(L-1)} \\ \hat{\boldsymbol{R}}_{\vec{\theta},1}^{(1)H} & \hat{\boldsymbol{R}}_{\vec{\theta},1}^{(0)} & \hat{\boldsymbol{R}}_{\vec{\theta},1}^{(1)} & \cdots & \hat{\boldsymbol{R}}_{\vec{\theta},1}^{(L-2)} \\ \hat{\boldsymbol{R}}_{\vec{\theta},1}^{(2)H} & \hat{\boldsymbol{R}}_{\vec{\theta},1}^{(1)H} & \hat{\boldsymbol{R}}_{\vec{\theta},1}^{(0)} & \cdots & \hat{\boldsymbol{R}}_{\vec{\theta},1}^{(L-3)} \\ \vdots & \vdots & \vdots & \ddots & \vdots \\ \hat{\boldsymbol{R}}_{\vec{\theta},1}^{(L-1)H} & \hat{\boldsymbol{R}}_{\vec{\theta},1}^{(L-2)H} & \hat{\boldsymbol{R}}_{\vec{\theta},1}^{(L-3)H} & \cdots & \hat{\boldsymbol{R}}_{\vec{\theta},1}^{(0)} \end{bmatrix} \tag{6.5}$$

The diagonal matrices are simply the spatial-only correlation matrices, which are the same as $\hat{\boldsymbol{R}}_{\vec{\theta},1}$. The small number in parenthesis denotes the number of samples that the data set is being time-shifted relative to itself in forming the space-time matrix. Specifically, it can be defined as:

$$\hat{\boldsymbol{R}}_{\vec{\theta},1}^{(k)}=\frac{1}{Q}\cdot\sum_{n=1}^{Q}\vec{z}_{\vec{\theta},1}[n]\cdot\vec{z}_{\vec{\theta},1}^{H}[n-k] \tag{6.6}$$

The off-diagonal matrices $\hat{\boldsymbol{R}}_{\vec{\theta},1}^{(k)}$ with $k>0$ provides the correlation among the signals not only from one antenna element to another but also at k samples apart.

For a wide-band source with no multi-path scattering, the auto-correlation and cross-correlation functions of the signals are simply a very narrow pulse. In other words, the data samples are practically uncorrelated from one sample to any next sample. Therefore, the off-diagonal matrices in the big space-time covariance matrix are all zero matrices. Each of the diagonal matrices, as mentioned earlier, has a rank of at least one; more if the signals are spatially decorrelated. Thus, the space-time covariance matrix has a rank of at least L. The signals can become spatially decorrelated when the multi-path

scattering is very severe or multiple jamming sources are present. In this case, the rank of the space-time covariance matrix will be more than L.

Decomposing the matrices into eigenvalues and eigenvectors reveals that the number of big eigenvalues for an L-tap space-time covariance matrix is typically L. The next two pages show some plots of the eigenvalues in dB for all azimuth angles. The plots are from one-tap, 3-tap, and 5-tap covariance matrices of the F-16 data at a depression angle of 10 degrees. Note that the top curve also corresponds to the power of the signal as a function of azimuth.

It was estimated from the results of equalization that the SNR is as low as 35 dB. Therefore, it is reasonable to say that those eigenvalues 35 dB or more below the peak power are due to noise. The small eigenvalues above this cut-off are attributed to the multi-path scattering. As mentioned earlier, for each depression angle, the attenuation settings have been picked so that the peak power is as high as possible but without saturating the A/D. Thus, all the peak power from different depression angles before being scaled to its absolute level are about the same. As a general rule, all eigenvalues having magnitudes less than 30 dB can be set to 0 ($-\infty$ dB) when reforming the covariance matrix from the eigenvalues and eigenvectors.

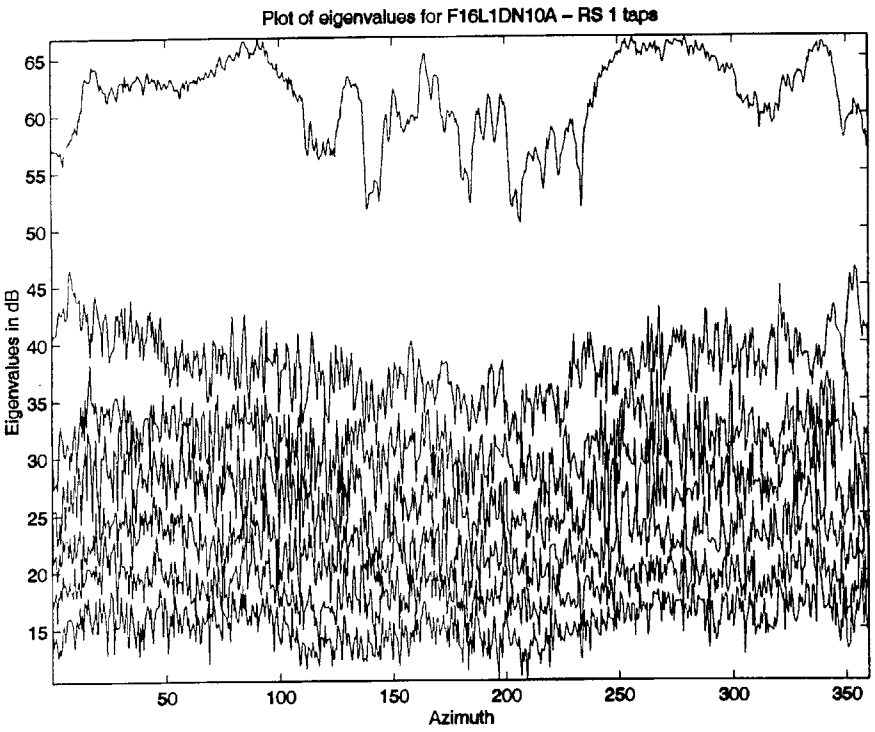

Figure 6.1: Plot of Eigenvalues - 1 tap

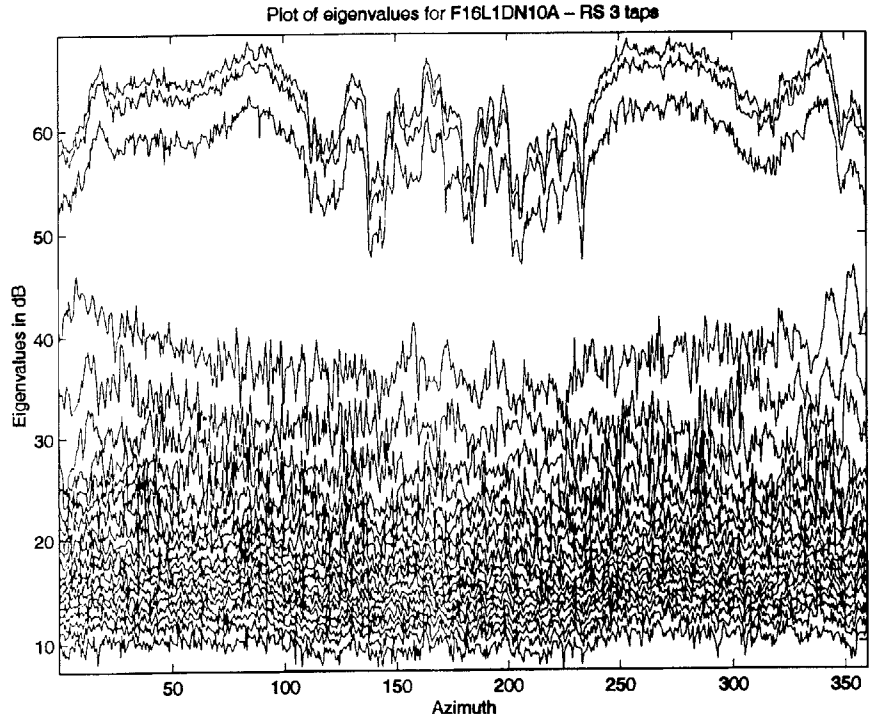

Figure 6.2: Plot of Eigenvalues - 3 taps

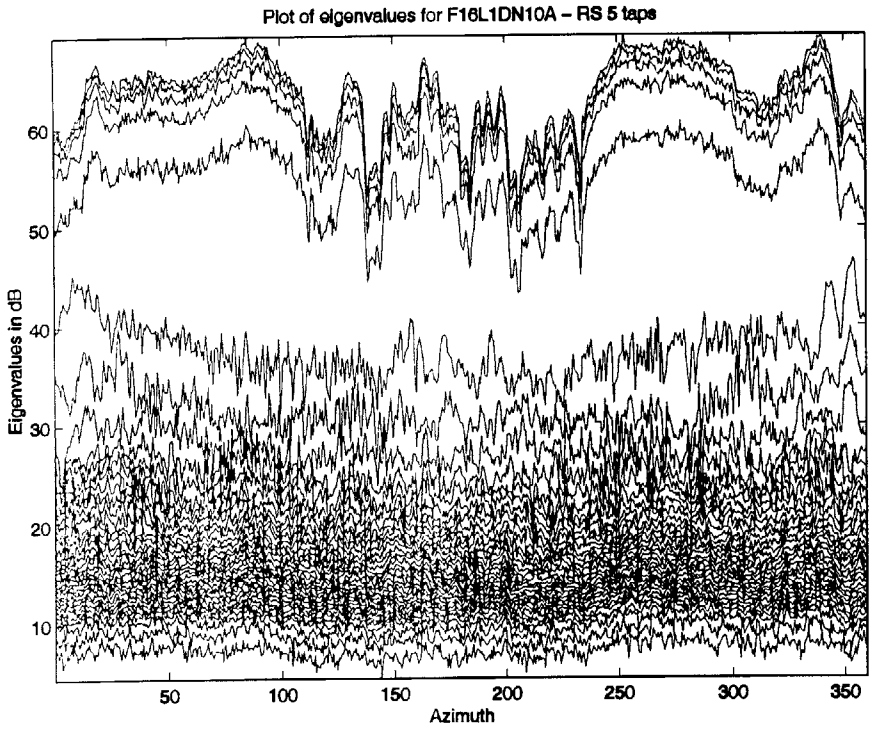

Figure 6.3: Plot of Eigenvalues - 5 taps

7 Simulating Jamming Signals

With all the space-time covariance matrices available, it is now possible to simulate jamming signals that have the same space-time correlation as specified by the matrices. The basic procedure involves the factorization of the Hermitian covariance matrix. For example, to simulate a jamming signal coming from a particular azimuth and depression, the corresponding matrix $\hat{\boldsymbol{R}}_{\vec{\theta}}$ is first selected for the desired number of taps L. It can then be factored into $\boldsymbol{B}$ and $\boldsymbol{B}^{H}$ as follows:

$$\boldsymbol{B} \cdot \boldsymbol{B}^{H} = \hat{\boldsymbol{R}}_{\vec{\theta}} \tag{7.1}$$

The size of $\boldsymbol{B}$ is $7L \times 7L$ which is the same as $\hat{\boldsymbol{R}}_{\vec{\theta}}$. The matrix $\boldsymbol{B}$ is next multiplied by a matrix $\boldsymbol{M}$ of independent zero-mean unit-variance Gaussian samples. A new matrix is obtained as follows:

$$\boldsymbol{Y} = \boldsymbol{B} \cdot \boldsymbol{M} \tag{7.2}$$

where $\boldsymbol{M}$ has a size of $7L \times (N/L)$ with N being the desired length of the final data sequence. The matrix $\boldsymbol{Y}$ will, of course, have a size of $7L \times (N/L)$. If the correlation matrix of the newly generated data $\boldsymbol{Y}$ is computed, it will be the following:

$$\begin{aligned} \boldsymbol{R}_{Y} &= \boldsymbol{Y} \cdot \boldsymbol{Y}^{H} \\ &= (\boldsymbol{B} \cdot \boldsymbol{M}) \cdot (\boldsymbol{B} \cdot \boldsymbol{M})^{H} \\ &= \boldsymbol{B} \cdot (\boldsymbol{M} \cdot \boldsymbol{M}^{H}) \cdot \boldsymbol{B}^{H} \\ &= \boldsymbol{B} \cdot \boldsymbol{B}^{H} \\ &= \hat{\boldsymbol{R}}_{\vec{\theta}} \end{aligned} \tag{7.3}$$

The result is the same as the original covariance matrix which is the characterization wanted in the generated data. Note that in the derivation, $(\boldsymbol{M} \cdot \boldsymbol{M}^{H}) = \boldsymbol{I}$, the identity matrix, since $\boldsymbol{M}$ is composed of independent Gaussian samples.

For $L > 1$, $\boldsymbol{Y}$ is rearranged to become the simulated data $\boldsymbol{X}$ as a $7 \times N$ matrix. The process is simply the reversal of that being described in Equation 6.2. It can be shown as follows:

$$X = [Y_{(7L-6:7L,1)} \quad \cdots \quad Y_{(8:14,1)} \quad Y_{(1:7,1)} \quad Y_{(7L-6:7L,2)} \quad \cdots \quad Y_{(8:14,2)} \quad Y_{(1:7,2)} \quad \cdots] \tag{7.4}$$

To obtain the factor $\boldsymbol{B}$ as required in Equation 7.1, the matrix $\hat{\boldsymbol{R}}_{\tilde{\theta}}$ is first decomposed into the following:

$$\boldsymbol{V} \cdot \boldsymbol{D} \cdot \boldsymbol{V}^{H} = \hat{\boldsymbol{R}}_{\tilde{\theta}} \tag{7.5}$$

where the columns of $\boldsymbol{V}$ are the eigenvectors of $\hat{\boldsymbol{R}}_{\tilde{\theta}}$ and the diagonal elements of the diagonal matrix $\boldsymbol{D}$ are the corresponding eigenvalues. Equation 7.5 is really the matrix form of what being introduced in Equation 6.3. It is important to note that the matrix $\boldsymbol{V}$ is an orthonormal matrix. An orthonormal matrix is a square matrix that has the property of $\boldsymbol{V}^{H} \cdot \boldsymbol{V} = \boldsymbol{V} \cdot \boldsymbol{V}^{H} = \boldsymbol{I}$, the identity matrix. Although the eigenvectors are all complex, the eigenvalues are all real. These essential properties of $\boldsymbol{V}$ and $\boldsymbol{D}$ enable finding a simple expression of $\boldsymbol{B}$ in terms of $\boldsymbol{V}$ and $\boldsymbol{D}$ themselves.

Next, let's define $\sqrt{\boldsymbol{D}}$ such that $\sqrt{\boldsymbol{D}} \cdot \sqrt{\boldsymbol{D}}^{H} = \boldsymbol{D}$. The expression for $\sqrt{\boldsymbol{D}}$ is simply the square roots of the diagonal elements of $\boldsymbol{D}$. That is,

$$\sqrt{\boldsymbol{D}} \equiv \begin{bmatrix} \sqrt{\lambda_1} & 0 & \cdots & 0 \\ 0 & \sqrt{\lambda_2} & \cdots & 0 \\ \vdots & \vdots & \ddots & \vdots \\ 0 & 0 & \cdots & \sqrt{\lambda_{7L}} \end{bmatrix} \tag{7.6}$$

where the λ_i's are the eigenvalues on the diagonal of $\boldsymbol{D}$. Note that because the λ_i's are real, $\sqrt{\boldsymbol{D}}$ is equal to $\sqrt{\boldsymbol{D}}^{\boldsymbol{H}}$.

Now, $\hat{\boldsymbol{R}}_{\tilde{\theta}}$ can be rewritten in another form as follows:

$$\begin{aligned}
\hat{\boldsymbol{R}}_{\tilde{\theta}} &= \boldsymbol{V}\cdot\boldsymbol{D}\cdot\boldsymbol{V}^{\boldsymbol{H}} && \text{(same as 7.5)} \\
&= \boldsymbol{V}\cdot\left(\sqrt{\boldsymbol{D}}\cdot\sqrt{\boldsymbol{D}}^{\boldsymbol{H}}\right)\cdot\boldsymbol{V}^{\boldsymbol{H}} && \text{(using } \sqrt{\boldsymbol{D}}\cdot\sqrt{\boldsymbol{D}}^{\boldsymbol{H}} = \boldsymbol{D}\text{)} \\
&= \boldsymbol{V}\cdot\sqrt{\boldsymbol{D}}\cdot\left(\boldsymbol{V}^{\boldsymbol{H}}\cdot\boldsymbol{V}\right)\cdot\sqrt{\boldsymbol{D}}^{\boldsymbol{H}}\cdot\boldsymbol{V}^{\boldsymbol{H}} && \text{(using } \boldsymbol{V}^{\boldsymbol{H}}\cdot\boldsymbol{V} = \boldsymbol{I}\text{)} \\
&= \left(\boldsymbol{V}\cdot\sqrt{\boldsymbol{D}}\cdot\boldsymbol{V}^{\boldsymbol{H}}\right)\cdot\left(\boldsymbol{V}\cdot\sqrt{\boldsymbol{D}}\cdot\boldsymbol{V}^{\boldsymbol{H}}\right)^{\boldsymbol{H}} && \text{(by regrouping terms)} \quad (7.7)
\end{aligned}$$

Matching the expression in (7.7) with the expression in (7.1) reveals $\boldsymbol{B}$ to be:

$$\boldsymbol{B} = \boldsymbol{V}\cdot\sqrt{\boldsymbol{D}}\cdot\boldsymbol{V}^{\boldsymbol{H}} \qquad (7.8)$$

The above analysis shows how to generate data having a pre-specified correlation matrix $\hat{\boldsymbol{R}}_{\tilde{\theta}}$. As a reminder, $\hat{\boldsymbol{R}}_{\tilde{\theta}}$ is computed from the complex experimental data. In practice, the desired correlation matrix is really a modified version of $\hat{\boldsymbol{R}}_{\tilde{\theta}}$. The reason for not using $\hat{\boldsymbol{R}}_{\tilde{\theta}}$ is that this matrix includes not only the multi-path characteristics but also the effects of noise from the experimental data. In order to simulate a noise-free jamming signal, $\hat{\boldsymbol{R}}_{\tilde{\theta}}$ will have to be modified. Looking at Figure 6.1, 6.2, and 6.3, it is observed that the small eigenvalues near the bottom are due to noise and the top ones are due to the multi-path effects. As discussed in the end of the previous chapter, a good rule of thumb based on the estimated SNR would be keeping only the eigenvalues above the 30 to 35 dB cut-off. The remaining eigenvalues are set to zero. In Equation 6.3, it is shown how a

Hermitian covariance matrix can be expressed in terms of its eigenvalues and eigenvectors. Here, the modified covariance matrix is formed in the same manner except that some of the lowest eigenvalues are set to zeros. The modified matrix is simply the following:

$$\boldsymbol{R}_{\vec{\theta}} = \sum_{i=1}^{K} \lambda_i \cdot \vec{\boldsymbol{v}}_i \cdot \vec{\boldsymbol{v}}_i^{\boldsymbol{H}} \tag{7.9}$$

where $\{1,..,K\}$ is the selected non-zero set of eigenvalues of descending magnitudes.

In matrix form, $\boldsymbol{R}_{\vec{\theta}}$ is:

$$\boldsymbol{R}_{\vec{\theta}} = \boldsymbol{V} \cdot \boldsymbol{D} \cdot \boldsymbol{P} \cdot \boldsymbol{V}^{\boldsymbol{H}} \tag{7.10}$$

where $\boldsymbol{P}$ is a diagonal matrix with the first K diagonal elements being 1's and the remaining diagonal elements being 0's.

With the additional term of $\boldsymbol{P}$, it can still be shown similarly as in (7.7) that the resulting $\boldsymbol{B}$ resembles (7.8) but includes $\boldsymbol{P}$. Namely, the actual $\boldsymbol{B}$ being used is:

$$\boldsymbol{B} = \boldsymbol{V} \cdot \sqrt{\boldsymbol{D}} \cdot \boldsymbol{P} \cdot \boldsymbol{V}^{\boldsymbol{H}} \tag{7.11}$$

The basic ideas have been presented for generating simulated jammers that correspond to a particular angle of arrival using the covariance matrices from the experimental data. The generated data $\boldsymbol{X}$ is then scaled appropriately according to the chosen parameters such as the power of the jammer source and the distance between the jammer and the receiver. Depending on the azimuth and depression of the simulated jammer, the power of the data is also scaled by the antenna gain which is a function of arrival angles. The antenna gain, with the antenna located on top of the aircraft, can be computed from the experimental data. This information is incorporated for every simulated jamming signal. As expected, the gains are much smaller at angles where the

jamming signals can be blocked by the wings or the tails. In general, the gain is smaller at a deeper depression angle. The next chapter will present the details for computing the gain along with some plots of the results. To further simulate an environment of multiple jammers, data obtained from different individual jammers are simply summed together to form the data for this more interesting scenario. The procedure is considered appropriate if one assumes that the jammers are practically uncorrelated with one another.

8 Computing Antenna Gain

Computing the actual antenna gain is based on the same Figure 3.1, which is shown here again.

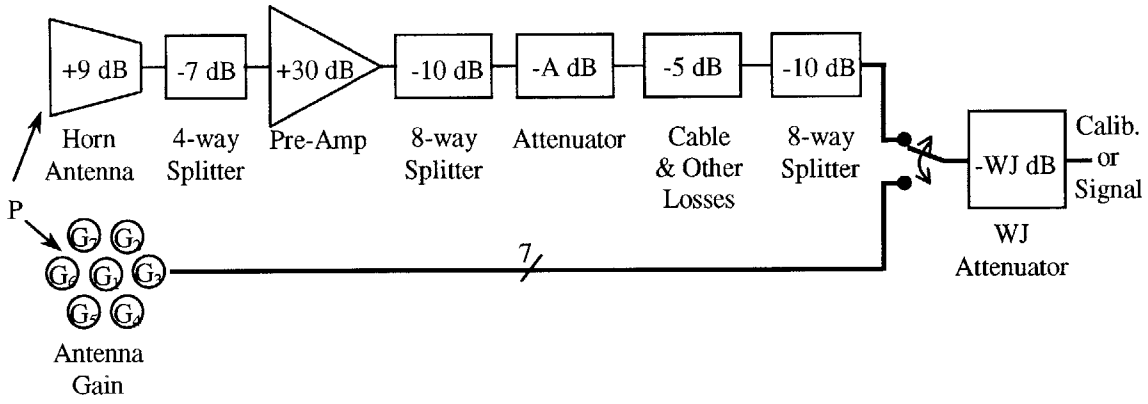

Figure 8.1: Attenuation Paths

The calibration power is:

$$P_c = P_0 + 9 - 7 + 30 - 10 - A - 5 - 10 - WJ + X$$
$$= P_0 - A + 7 - WJ + X \quad [dB] \tag{8.1}$$

Likewise, the signal power is:

$$P_s = P_0 + G - WJ + X \quad [dB] \tag{8.2}$$

where P_0 is the same power for both the calibration and the signal; X is the constant conversion factor from the analog signal power to the discrete signal power. Solving for the antenna gain G results in the following expression:

$$G = (P_s - P_c) - A + 7 \quad [dB] \tag{8.3}$$

The average antenna gain (average of 7 elements) is plotted on the next two pages for the F-16 and F-15 data, at both L_1 and L_2 frequencies.

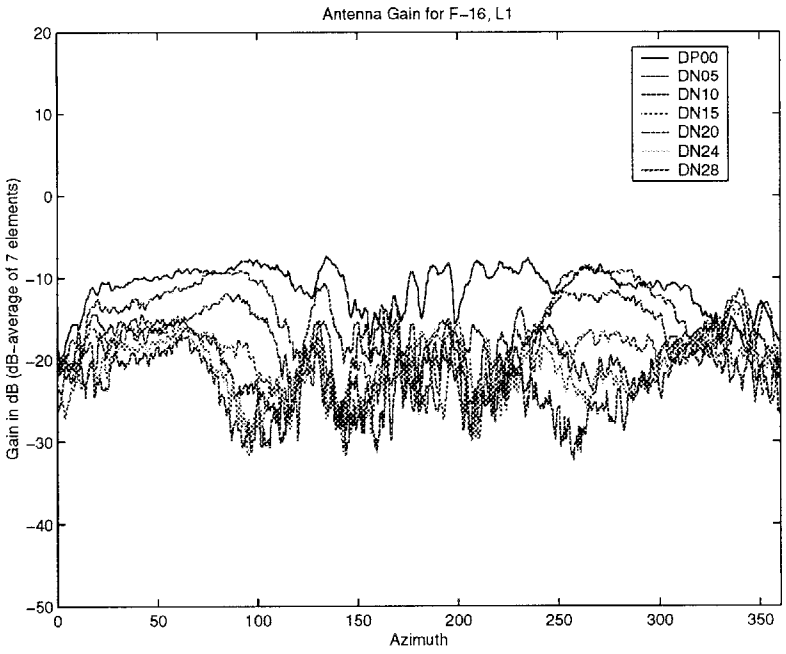

Figure 8.2: Antenna Gain for F-16, L_1

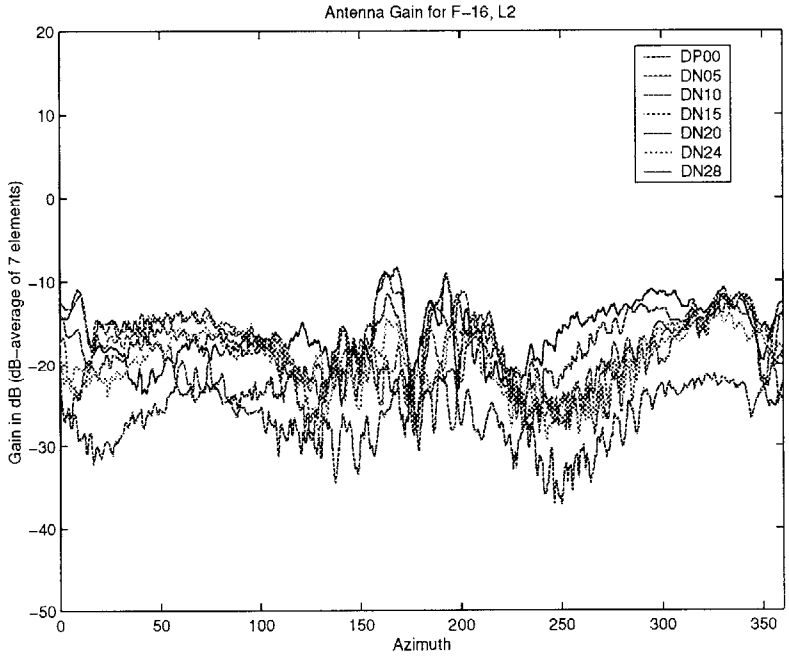

Figure 8.3: Antenna Gain for F-16, L_2

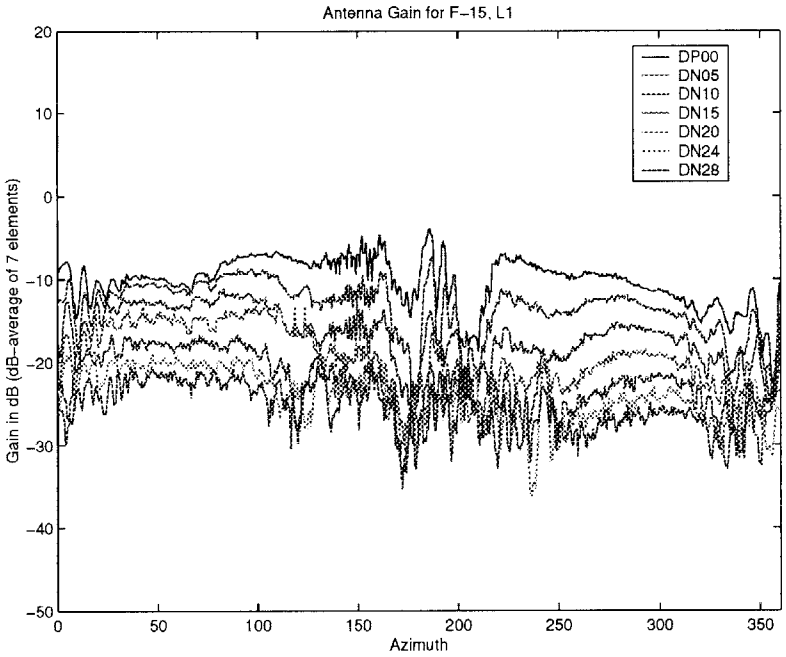

Figure 8.4: Antenna Gain for F-15, L_1

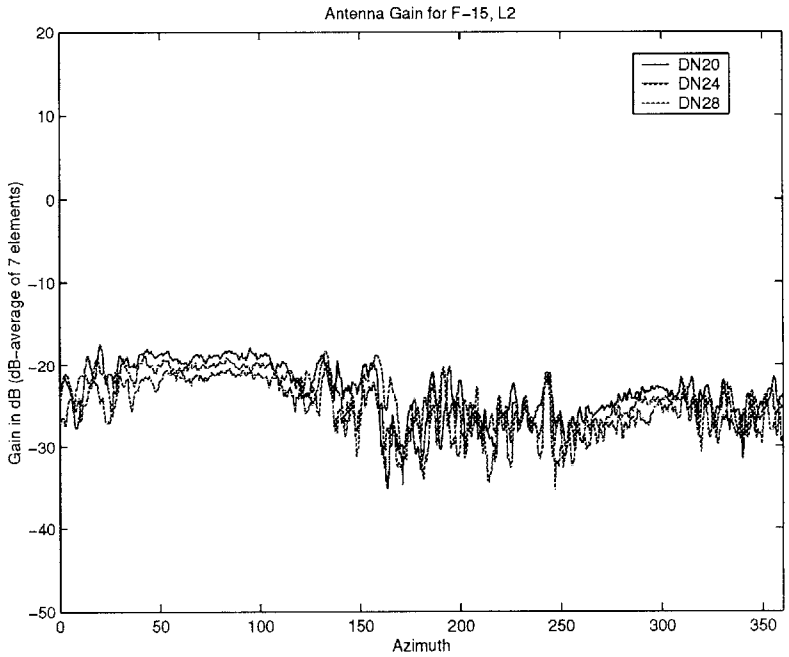

Figure 8.5: Antenna Gain for F-15, L_2

9 Space-Time Adaptive Beamforming[1]

9.1 Overview

A near-field multi-path scatterer can be modeled as a scaled and delayed version of the direct-path jammer, but with a different direction of arrival. Due to the delay, the direct-path jammer and its single multi-path reflection are only partially correlated. As a result, the covariance matrix for this simple case will have a rank of two. If more multi-path scatterers are present, the rank of the covariance matrix will increase by the number of additional scatterers. A conventional spatial beamformer might not have enough degrees of freedom to deal with excessive multi-path scatterers. The spatial beamformer allows only one complex weight per channel, thus the only freedom is to adjust the gain and phase of each channel. For the simple case of no multi-path scattering, the signals from different antenna elements are identical except for the gain and phase. A single complex weight per channel is then sufficient for nulling the jamming signals while preserving the desired GPS signal from a different direction. However, when multiple delayed and attenuated replicas of the jammer show up from various directions in addition to the direct jammer, the received signals become decorrelated from one channel to another and appear more like noise. It is then difficult for the spatial beamformer to select the weights such that the signals would add up destructively. The apparent solution is to allow more than one time-tap per channel so that the signals can also be delayed to cancel out its replicas.

[1] The derivations for the algorithms are based on the hand-written notes of Dr. Gary Hatke and his paper titled "Adaptive Array Processing for Wide-band Nulling in GPS Systems."

The space-time adaptive processor (STAP) is introduced to solve this partially correlated multi-path problem. The idea is to use the tapped delay lines to provide sufficient delay so that the multi-path component of received signal can easily be correlated with the direct-path jammer. Consequently, they can be made to cancel each other out with appropriately chosen weights. The diagram below illustrates the structure of a space-time adaptive processor.

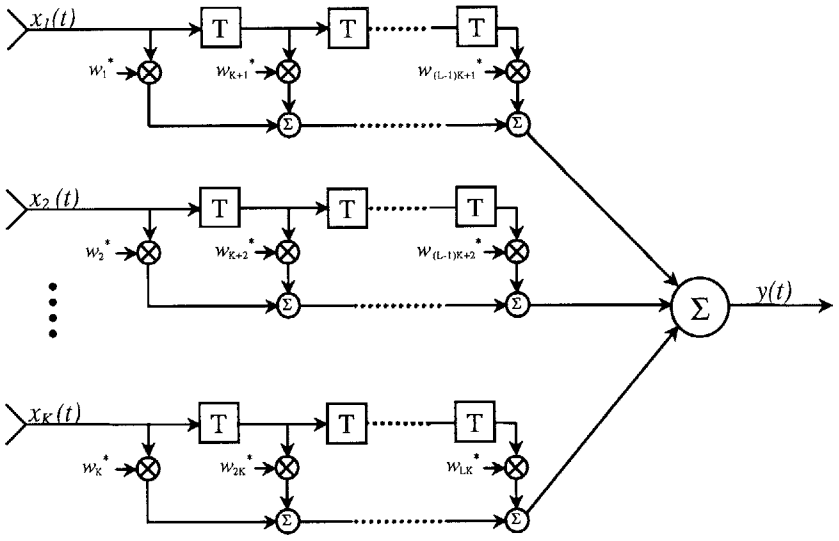

Figure 9.1: The Space-Time Adaptive Processor

It is crucial to choose the number of delays (L-1) such that the total delay of one tapped delay line must exceed the expected range of delays of the multi-path scatterers. At the sampling rate of 25.6 MHz, each sampling period T is about 40 nano-seconds. Thus with one additional *complex* tap, the direct jammer and its scatterer can be correlated for a delay of up to 80 ns. An 80 ns delay would also translate into an extra distance of roughly 80 feet that the replica signal has to travel. Given the physical size of the aircraft, the additional path for the scatterers can be said to be no more than 80 feet. Therefore, one tap spacing (i.e. L = 2 taps) is quite sufficient to cover the whole delay

range. However, given the arbitrary delays of the scatterers, the processor must also be able to approximate non-integer delays in a discrete system. Clearly, the more taps used in the tapped delay line would provide the additional flexibility for a more effective implementation. Yet, when a sufficient number of taps is used, the performance will approach some asymptotic limit. The optimum number of taps must be determined to minimize any unnecessary computation. In the actual evaluation of the algorithms, the performance of the spatial-only processor ($L = 1$) is compared with that of the space-time processor for cases with $L = 3$ and 5.

9.2 Computing the Optimal Weights

The optimum weights are computed such that the signal-to-interference-plus-noise ratio (SINR) is maximized. The general form of the solution is based on the Wiener-Hoft equation which is given as follows:

$$\vec{w}_l = \boldsymbol{R}_{st}^{-1} \cdot \vec{r}_l(\vec{\gamma}) \tag{9.1}$$

where $\vec{w}_l$ is the weight vector $\begin{bmatrix} w_1 \\ w_2 \\ \vdots \\ w_{LK} \end{bmatrix}$, $\boldsymbol{R}_{st}$ is the $LK \times LK$ space-time covariance matrix of the received interference plus noise signals, and $\vec{r}_l(\vec{\gamma})$ is the space-time cross-correlation vector between the received signals and the desired signal from the lth satellite. The space-time covariance matrix is defined similarly as in Equation 6.2. The cross-correlation vector for a spatial-only processor is simply the array propagation vector as follows:

$$\vec{r}_l = \vec{v}_l = \begin{bmatrix} 1 \\ e^{j\cdot\phi_2} \\ \vdots \\ e^{j\cdot\phi_K} \end{bmatrix} \tag{9.2}$$

where $\phi_2 \ldots \phi_K$ are the phase delay with respect to the first array element. For a space-time processor, the cross-relation vector $\vec{r}_l(\vec{\gamma})$ is made up of L copies of the same but unequally scaled array propagation vectors. The general form of $LK \times 1$ is as follows:

$$\vec{r}_l(\vec{\gamma}) = \begin{bmatrix} \gamma_1 \vec{v}_l \\ \gamma_2 \vec{v}_l \\ \vdots \\ \gamma_L \vec{v}_l \end{bmatrix} \tag{9.3}$$

where $\gamma_1 \ldots \gamma_L$ are chosen specifically to meet certain constraints while SINR is being maximized.

The need for constraints is due to the effect of having a tap delay line for each of the channels. At the output of a space-time adaptive processor, the GPS signals would have been not only spatially weighted, but also been filtered by an effective FIR. Thus, the phase and delay of the GPS signals could have been significantly altered. Since the relative phase and delay difference among the GPS signals are very important in calculating user position, it is undesirable to corrupt these phases and introduce false group delay. However, one can specify that all the beamformers steering toward the GPS satellites must have the identical group delay in their effective FIR's. This specification in effect guarantees that the differences in delay among the signals are unchanged by the processors. To meet this requirement, three different constraints are proposed for three different algorithms resulting in comparable performance. The three algorithms are similar except that each constraint governs a different computation and selection of γ's.

A weight matrix $\boldsymbol{W}_l$ are defined from the weights in Figure 9.1 following the same arrangement:

$$\boldsymbol{W}_l \equiv \begin{bmatrix} w_1 & w_{K+1} & \cdots & w_{(L-1)K+1} \\ w_2 & w_{K+2} & \cdots & w_{(L-1)K+2} \\ \vdots & \vdots & \ddots & \vdots \\ w_K & w_{2K} & \cdots & w_{LK} \end{bmatrix} \tag{9.4}$$

Since the GPS signal has different propagation phase delay to other antenna elements with respect to the first element, the effective FIR filter for the l^{th} satellite signal is then the weight matrix $\boldsymbol{W}_l$ multiplied with the propagation vector $\vec{\boldsymbol{v}}_l$ as follows:

$$\vec{\boldsymbol{h}}_l = (\vec{\boldsymbol{v}}_l^T \cdot \boldsymbol{W}_l^*)^T = \boldsymbol{W}^H \cdot \vec{\boldsymbol{v}}_l \tag{9.5}$$

Alternately, $\vec{\boldsymbol{h}}_l$ can be expressed in term of the weight vector $\vec{\boldsymbol{w}}_l$ as:

$$\vec{\boldsymbol{h}}_l = \boldsymbol{V}_l^T \cdot \vec{\boldsymbol{w}}_l^* = \boldsymbol{V}_l^T \cdot (\boldsymbol{R}_{st}^{-1} \cdot \vec{\boldsymbol{r}}_l(\vec{\gamma}))^* \tag{9.6}$$

where $\boldsymbol{V}_l$ is defined as:

$$\boldsymbol{V}_l \equiv \boldsymbol{I}_L \otimes \vec{\boldsymbol{v}}_l = \begin{bmatrix} \vec{\boldsymbol{v}}_l & \vec{\boldsymbol{0}} & \cdots & \vec{\boldsymbol{0}} \\ \vec{\boldsymbol{0}} & \vec{\boldsymbol{v}}_l & \cdots & \vec{\boldsymbol{0}} \\ \vdots & \vdots & \ddots & \vdots \\ \vec{\boldsymbol{0}} & \vec{\boldsymbol{0}} & \cdots & \vec{\boldsymbol{v}}_l \end{bmatrix} \tag{9.7}$$

The equation for the weight vector can be rewritten in term of the $L\times 1$ $\vec{\gamma}$ vector as follows:

$$\vec{\boldsymbol{w}}_l = \boldsymbol{R}_{st}^{-1} \cdot \begin{bmatrix} \gamma_1 \vec{\boldsymbol{v}}_l \\ \gamma_2 \vec{\boldsymbol{v}}_l \\ \vdots \\ \gamma_L \vec{\boldsymbol{v}}_l \end{bmatrix}$$

$$= \boldsymbol{R}_{st}^{-1} \cdot \boldsymbol{V}_l \cdot \vec{\gamma} \tag{9.8}$$

By substituting (9.8) into (9.6), an equivalent expression for the effective FIR can be obtained:

$$\begin{aligned}\vec{h}_l &= \boldsymbol{V}_l^T \cdot (\boldsymbol{R}_{st}^{-1} \cdot \boldsymbol{V}_l \cdot \vec{\gamma})^* \\ &= (\boldsymbol{V}_l^H \cdot \boldsymbol{R}_{st}^{-1} \cdot \boldsymbol{V}_l \cdot \vec{\gamma})^* \\ &= (\boldsymbol{M} \cdot \vec{\gamma})^* \end{aligned} \tag{9.9}$$

where the Hermitian matrix $\boldsymbol{M}$ is defined as:

$$\boldsymbol{M} \equiv \boldsymbol{V}_l^H \cdot \boldsymbol{R}_{st}^{-1} \cdot \boldsymbol{V}_l \tag{9.10}$$

It is seen from (9.9) that by choosing $\vec{\gamma}$ appropriately, the effective FIR can be constrained to having a particular desired property. The next three sections will elaborate on the selections of $\vec{\gamma}$.

9.2.1 The All-Pass Constraint

The all-pass constraint requires that the expression for $\vec{h}_l$ from (9.9) be set to an impulse so that its frequency response is an all-pass.

$$\vec{h}_l = (\boldsymbol{M} \cdot \vec{\gamma})^* = \begin{bmatrix} \vdots \\ 0 \\ 1 \\ 0 \\ \vdots \end{bmatrix} \tag{9.11}$$

Consequently, $\vec{\gamma}_{opt}$ is chosen to be:

$$\vec{\gamma}_{opt} = \boldsymbol{M}^{-1} \cdot \begin{bmatrix} \vdots \\ 0 \\ 1 \\ 0 \\ \vdots \end{bmatrix} \tag{9.12}$$

Once $\vec{\gamma}_{opt}$ is computed, the weight vector is found from Equation (9.8).

9.2.2 The Fixed-Delay Constraint

The fixed-delay constraint only requires that all effective FIR's have the same group delay, but not necessarily be an all-pass. By relaxing the constraint from the previous case, some improvement in performance can be expected. The goal here is to maximize the power of the GPS receiver correlation output at time $D \cdot \Delta T$ delayed from the true correlation peak subject to a fixed noise power.

The GPS signal component at the output of the processor is:

$$y(t) = \sum_{i=1}^{L} h_i \cdot s\left(t - (i-1) \cdot \Delta T\right) \tag{9.13}$$

where h_i's are the FIR coefficients in $\vec{h}_i$.

The correlator output is then:

$$\begin{aligned} R_{ys}(\tau) &= E\left\{y^*(t) \cdot s(t-\tau)\right\} \\ &= E\left\{\sum_{i=1}^{L} h_i^* \cdot s^*\left(t-(i-1)\cdot\Delta T\right) \cdot s\left(t-\tau\right)\right\} \end{aligned} \tag{9.14}$$

By defining a new vector $\vec{r}(\tau)$ as:

$$\begin{aligned} \vec{r}(\tau) &\equiv E\left\{\begin{bmatrix} s^*(t)\cdot s(t-\tau) \\ s^*(t-\Delta T)\cdot s(t-\tau) \\ \vdots \\ s^*(t-(L-1)\Delta T)\cdot s(t-\tau) \end{bmatrix}\right\} \\ &= E\left\{\begin{bmatrix} s^*(t)\cdot s(t-\tau) \\ s^*(t)\cdot s(t-(\tau-\Delta T)) \\ \vdots \\ s^*(t)\cdot s(t-(\tau-(L-1)\Delta T)) \end{bmatrix}\right\} \equiv \begin{bmatrix} R_{ss}(\tau) \\ R_{ss}(\tau-\Delta T) \\ \vdots \\ R_{ss}(\tau-(L-1)\Delta T) \end{bmatrix} \end{aligned} \tag{9.15}$$

Equation (9.14) can be rewritten simply as:

$$R_{ys}(\tau) = \vec{h}_i^H \cdot \vec{r}(\tau) \tag{9.16}$$

The quantity being maximized is the power of the correlator output:

$$\left|R_{ys}(\tau)\right|^2 = \vec{r}^{\,H}(\tau)\cdot\vec{h}_l\cdot\vec{h}_l^{\,H}\cdot\vec{r}(\tau) \tag{9.17}$$

If $\left|R_{ys}(\tau)\right|^2$ is to be maximized at some delay $\tau_0 = D\cdot\Delta T$, its partial derivative with respect to τ must be 0.

$$\left.\frac{\partial\left|R_{ys}(\tau)\right|^2}{\partial\tau}\right|_{\tau=\tau_0} = \frac{\partial\vec{r}^{\,H}(\tau)}{\partial\tau}\cdot\vec{h}_l\cdot\vec{h}_l^{\,H}\cdot\vec{r}(\tau) + \vec{r}^{\,H}(\tau)\cdot\vec{h}_l\cdot\vec{h}_l^{\,H}\cdot\left.\frac{\partial\vec{r}(\tau)}{\partial\tau}\right|_{\tau=\tau_0} = 0 \tag{9.18}$$

To satisfy the above equation, the following constraint is needed:

$$\vec{h}_l^{\,H}\cdot\frac{\partial\vec{r}(\tau_0)}{\partial\tau} = 0 \tag{9.19}$$

Using the expression for $\vec{h}_l$ from (9.9), the above equation becomes:

$$(\boldsymbol{M}\cdot\vec{\gamma})^T\cdot\frac{\partial\vec{r}(\tau_0)}{\partial\tau} = 0 \tag{9.20}$$

Recognizing that $\boldsymbol{M}$ is Hermitian and $\vec{r}(\tau_0)$ is real, (9.20) can be rearranged as:

$$\vec{\gamma}^{\,H}\cdot\left(\boldsymbol{M}\cdot\frac{\partial\vec{r}(\tau_0)}{\partial\tau}\right) = 0 \tag{9.21}$$

or denoted by the following orthogonality:

$$\vec{\gamma}\perp\vec{u} \tag{9.22}$$

where $\vec{u}$ is defined as:

$$\vec{u} \equiv \boldsymbol{M}\cdot\frac{\partial\vec{r}(\tau_0)}{\partial\tau} \tag{9.23}$$

A constrained optimization equation can now be set up for solving $\vec{\gamma}$. Recall that the objective is to maximize the power of the correlator output while keeping a constant interference noise power and having a fixed group delay.

Rewritten using (9.9), the correlator output power from Equation (9.17) becomes:

$$\left|R_{ys}(\tau_0)\right|^2 = \vec{\gamma}^H \cdot \boldsymbol{M}^H \cdot \vec{\boldsymbol{r}}(\tau_0) \cdot \vec{\boldsymbol{r}}^H(\tau_0) \cdot \boldsymbol{M} \cdot \vec{\gamma} \tag{9.24}$$

The output of the space-time processor is the following:

$$y[n] = \boldsymbol{w}^H \cdot \begin{bmatrix} \vec{x}[n] \\ \vec{x}[n-1] \\ \vdots \\ \vec{x}[n-(L-1)] \end{bmatrix} \equiv \boldsymbol{w}^H \cdot \boldsymbol{X} \tag{9.25}$$

where $\vec{x}[n]$ is a vector of K values from K antenna elements at time n.

If the GPS signal power is much weaker compared to the interference plus noise power, then the interference plus noise power is simply the output power:

$$\begin{aligned} E\{y \cdot y^*\} &= \frac{1}{N} \cdot \sum_{i=1}^{N} y[i] \cdot y^*[i] \\ &= \frac{1}{N}\left(\boldsymbol{w}_l^H \cdot \boldsymbol{X} \cdot \boldsymbol{X}^H \cdot \boldsymbol{w}_l\right) \\ &= \boldsymbol{w}_l^H \cdot \boldsymbol{R}_{st} \cdot \boldsymbol{w}_l \end{aligned} \tag{9.26}$$

In terms of $\vec{\gamma}$, (9.26) becomes:

$$\begin{aligned} E\{y \cdot y^*\} &= \left(\boldsymbol{R}_{st}^{-1} \cdot \boldsymbol{V}_l \cdot \vec{\gamma}\right)^H \cdot \boldsymbol{R}_{st} \cdot \left(\boldsymbol{R}_{st}^{-1} \cdot \boldsymbol{V}_l \cdot \vec{\gamma}\right) \\ &= \vec{\gamma}^H \cdot \boldsymbol{V}_l^H \cdot \boldsymbol{R}_{st}^{-1} \cdot \boldsymbol{R}_{st} \cdot \boldsymbol{R}_{st}^{-1} \cdot \boldsymbol{V}_l \cdot \vec{\gamma} \\ &= \vec{\gamma}^H \cdot \boldsymbol{M} \cdot \vec{\gamma} \end{aligned} \tag{9.27}$$

The signal to interference plus noise ratio (SINR) in terms of $\vec{\gamma}$ can now be obtained from (9.24) and (9.27). The problem is to solve for $\vec{\gamma}$ such the SINR is maximized, subject to the constraint specified by (9.22).

$$\max_{\gamma \perp \vec{u}} \frac{\vec{\gamma}^H \cdot \boldsymbol{M}^H \cdot \vec{\boldsymbol{r}}(\tau_0) \cdot \vec{\boldsymbol{r}}^H(\tau_0) \cdot \boldsymbol{M} \cdot \vec{\gamma}}{\vec{\gamma}^H \cdot \boldsymbol{M} \cdot \vec{\gamma}} \tag{9.28}$$

In order to simplify the problem, the basis for $\vec{\gamma}$ which is the subspace being orthogonal to $\vec{u}$ is first determined to be the following:

$$\boldsymbol{P} \equiv \left(\boldsymbol{I} - \frac{\vec{u} \cdot \vec{u}^{H}}{\vec{u}^{H} \cdot \vec{u}} \right) \cdot [\vec{e}_1 \quad \cdots \quad \vec{e}_{L-1}] \tag{9.29}$$

where $\boldsymbol{I}$ is an $L \times L$ identity matrix and $\vec{e}_1 \ldots \vec{e}_{L-1}$ are the first L-1 columns of $\boldsymbol{I}$.

A new vector $\vec{\tilde{\gamma}}$ of size $(L\text{-}1)\times 1$ is defined such that:

$$\vec{\gamma} = \boldsymbol{P} \cdot \vec{\tilde{\gamma}} \tag{9.30}$$

The expression of (9.30) can be substituted into (9.28) and the SINR can then be freely optimized over $\vec{\tilde{\gamma}}$ instead. Any solution found for $\vec{\tilde{\gamma}}$ can be projected back to $\vec{\gamma}$ via (9.30). The projection guarantees that $\vec{\gamma}$ is always in the orthogonal subspace of $\vec{u}$.

The new optimization expression is:

$$\max_{\vec{\tilde{\gamma}}} \frac{\vec{\tilde{\gamma}}^{H} \cdot \boldsymbol{P}^{H} \cdot \boldsymbol{M}^{H} \cdot \vec{r}(\tau_0) \cdot \vec{r}^{H}(\tau_0) \cdot \boldsymbol{M} \cdot \boldsymbol{P} \cdot \vec{\tilde{\gamma}}}{\vec{\tilde{\gamma}}^{H} \cdot \boldsymbol{P}^{H} \cdot \boldsymbol{M} \cdot \boldsymbol{P} \cdot \vec{\tilde{\gamma}}} \tag{9.31}$$

To put (9.31) into a Rayleigh Quotient form, the following definitions are used:

$$\vec{\beta} \equiv (\boldsymbol{P}^{H} \cdot \boldsymbol{M} \cdot \boldsymbol{P})^{\frac{1}{2}} \cdot \vec{\tilde{\gamma}} \tag{9.32}$$

$$\vec{\tilde{\gamma}} = (\boldsymbol{P}^{H} \cdot \boldsymbol{M} \cdot \boldsymbol{P})^{-\frac{1}{2}} \cdot \vec{\beta} \tag{9.33}$$

Expression (9.31) then becomes:

$$\max_{\vec{\beta}} \frac{\vec{\beta}^{H} \cdot (\boldsymbol{P}^{H} \cdot \boldsymbol{M} \cdot \boldsymbol{P})^{-\frac{1}{2}} \cdot \boldsymbol{P}^{H} \cdot \boldsymbol{M}^{H} \cdot \vec{r}(\tau_0) \cdot \vec{r}^{H}(\tau_0) \cdot \boldsymbol{M} \cdot \boldsymbol{P} \cdot (\boldsymbol{P}^{H} \cdot \boldsymbol{M} \cdot \boldsymbol{P})^{-\frac{1}{2}} \cdot \vec{\beta}}{\vec{\beta}^{H} \cdot \vec{\beta}} \tag{9.34}$$

or

$$\max_{\vec{\beta}} \frac{\vec{\beta}^{H} \cdot \boldsymbol{A} \cdot \boldsymbol{A}^{H} \cdot \vec{\beta}}{\vec{\beta}^{H} \cdot \vec{\beta}} \tag{9.35}$$

by defining:

$$\boldsymbol{A}^H \equiv \vec{\boldsymbol{r}}^H(\tau_0) \cdot \boldsymbol{M} \cdot \boldsymbol{P} \cdot (\boldsymbol{P}^H \cdot \boldsymbol{M} \cdot \boldsymbol{P})^{-\frac{1}{2}} \tag{9.36}$$

The maximum of (9.35) is $\left\| \boldsymbol{A} \cdot \boldsymbol{A}^H \right\|$ by the definition of the norm of a matrix. In this simple case where $\boldsymbol{A}$ is a column vector, $\left\| \boldsymbol{A} \cdot \boldsymbol{A}^H \right\|$ has a value of $\boldsymbol{A}^H \cdot \boldsymbol{A}$. Thus, it can be found by inspection that:

$$\vec{\beta}_{opt} = \boldsymbol{A} = (\boldsymbol{P}^H \cdot \boldsymbol{M} \cdot \boldsymbol{P})^{-\frac{1}{2}} \cdot \boldsymbol{P}^H \cdot \boldsymbol{M}^H \cdot \vec{\boldsymbol{r}}(\tau_0) \tag{9.37}$$

Then,

$$\begin{aligned} \vec{\tilde{\gamma}}_{opt} &= (\boldsymbol{P}^H \cdot \boldsymbol{M} \cdot \boldsymbol{P})^{-\frac{1}{2}} \cdot \vec{\beta}_{opt} \\ &= (\boldsymbol{P}^H \cdot \boldsymbol{M} \cdot \boldsymbol{P})^{-1} \cdot \boldsymbol{P}^H \cdot \boldsymbol{M}^H \cdot \vec{\boldsymbol{r}}(\tau_0) \end{aligned} \tag{9.38}$$

Finally,

$$\begin{aligned} \vec{\gamma}_{opt} &= \boldsymbol{P} \cdot \vec{\tilde{\gamma}}_{\text{opt}} \\ &= \boldsymbol{P} \cdot (\boldsymbol{P}^H \cdot \boldsymbol{M} \cdot \boldsymbol{P})^{-1} \cdot \boldsymbol{P}^H \cdot \boldsymbol{M}^H \cdot \vec{\boldsymbol{r}}(\tau_0) \end{aligned} \tag{9.39}$$

In evaluating the expression for $\vec{\gamma}$, two functions are needed: the auto-correlation of the GPS signal and its derivative. If the flat spectrum of the GPS signal is low-passed with a cut-off frequency of ω_0, the discrete auto-correlation function can be derived to be the following:

$$\boldsymbol{R}_{ss}[k] = \frac{\sin(\omega_0 \cdot k)}{(\omega_0 \cdot k)} \tag{9.40}$$

And its derivative is then:

$$\frac{\partial \boldsymbol{R}_{ss}[k]}{\partial k} = \frac{\cos(\omega_0 \cdot k)}{k} - \frac{\sin(\omega_0 \cdot k)}{\omega_0 \cdot k^2} \tag{9.41}$$

Plots of Equations (9.40) and (9.41) are shown below for $\omega_0 = \frac{10}{12} \cdot \pi$. The continuous waveforms are also included to show where the samples are taken from.

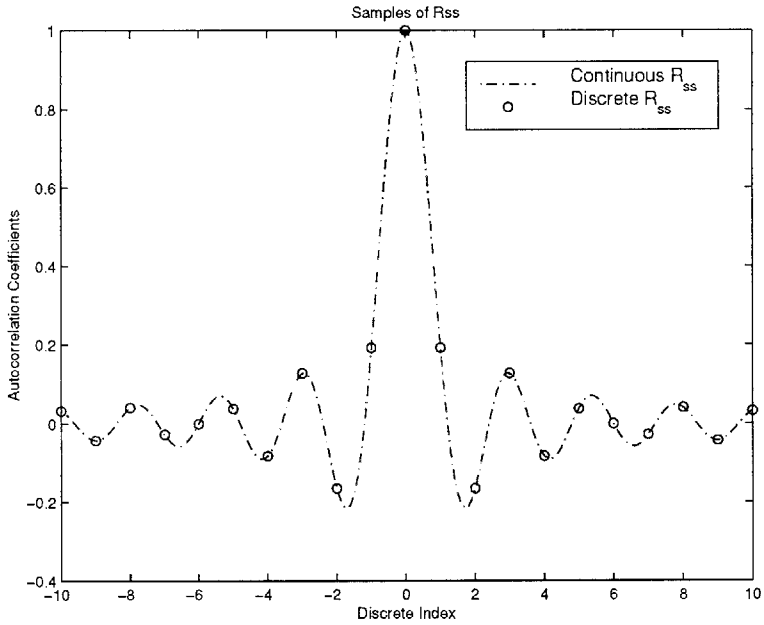

Figure 9.2: GPS Auto-correlation Function

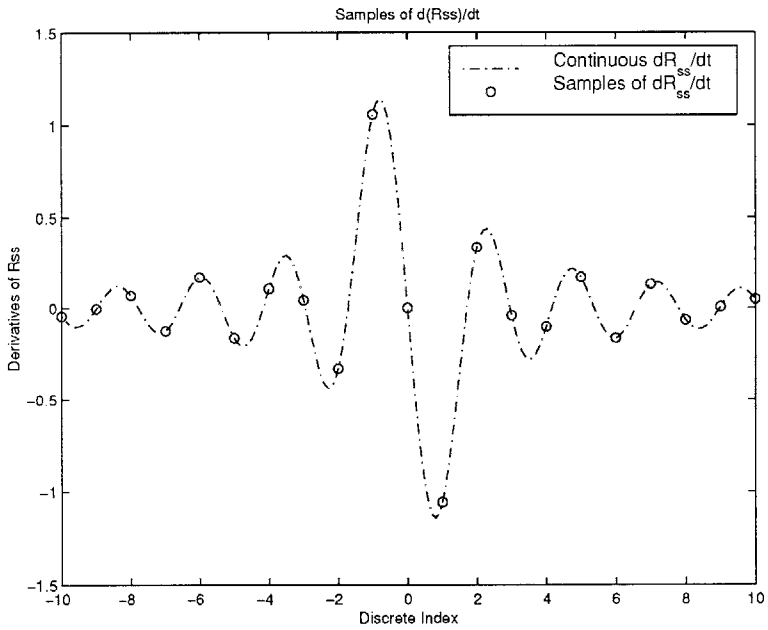

Figure 9.3: Derivative of GPS Auto-correlation

9.2.3 The Equalization Method

In this method, $\vec{\gamma}$ can be freely selected when maximizing the SINR. Without any constraint on $\vec{\gamma}$, the group delay clearly will be different from one beam output to another. The way to account for the random delay is to equalize the output signal with the effective FIR's from all other beams. Effectively, the overall filter is identical for every beam.

The set-up for solving $\vec{\gamma}$ is the same as Equation (9.28), except that there is no constraint on $\vec{\gamma}$.

$$\max_{\vec{\gamma}} \frac{\vec{\gamma}^H \cdot \boldsymbol{M}^H \cdot \vec{\boldsymbol{r}}(\tau_0) \cdot \vec{\boldsymbol{r}}^H(\tau_0) \cdot \boldsymbol{M} \cdot \vec{\gamma}}{\vec{\gamma}^H \cdot \boldsymbol{M} \cdot \vec{\gamma}} \tag{9.42}$$

Using the same approach as before, (9.42) can be rewritten as:

$$\max_{\vec{\beta}} \frac{\vec{\beta}^H \cdot \boldsymbol{M}^{\frac{1}{2}} \cdot \vec{\boldsymbol{r}}(\tau_0) \cdot \vec{\boldsymbol{r}}^H(\tau_0) \cdot \boldsymbol{M}^{\frac{1}{2}} \cdot \vec{\beta}}{\vec{\beta}^H \cdot \vec{\beta}} \tag{9.43}$$

by defining:

$$\vec{\beta} \equiv \boldsymbol{M}^{\frac{1}{2}} \cdot \vec{\gamma} \tag{9.44}$$

and

$$\vec{\gamma} = \boldsymbol{M}^{-\frac{1}{2}} \cdot \vec{\beta} \tag{9.45}$$

The solution to (9.43) is seen to be:

$$\vec{\beta}_{opt} = \boldsymbol{M}^{\frac{1}{2}} \cdot \vec{\boldsymbol{r}}(\tau_0) \tag{9.46}$$

It then follows that:

$$\begin{aligned} \vec{\gamma}_{opt} &= \boldsymbol{M}^{-\frac{1}{2}} \cdot \boldsymbol{M}^{\frac{1}{2}} \cdot \vec{\boldsymbol{r}}(\tau_0) \\ &= \vec{\boldsymbol{r}}(\tau_0) \end{aligned} \tag{9.47}$$

The beam equalization is carried out by convolving each beam output with a filter $\vec{f}$. The four equalization filters for four beams are given as:

$$\vec{f}_1 = \vec{h}_2 * \vec{h}_3 * \vec{h}_4 \tag{9.48}$$

$$\vec{f}_2 = \vec{h}_1 * \vec{h}_3 * \vec{h}_4 \tag{9.49}$$

$$\vec{f}_3 = \vec{h}_1 * \vec{h}_2 * \vec{h}_4 \tag{9.50}$$

$$\vec{f}_4 = \vec{h}_1 * \vec{h}_2 * \vec{h}_3 \tag{9.51}$$

As a result, all beams will have the identical overall filter as the following:

$$\vec{h}_{eff} = \vec{h}_1 * \vec{h}_2 * \vec{h}_3 * \vec{h}_4 \tag{9.52}$$

9.3 Simulation Results

The F-15, L_1 frequency IQ data are used in the following simulation. The simulation is set up such that one GPS satellite is directly overhead and three other GPS satellites are at 15 ° above the horizon, evenly spaced at 47 °, 167 °, and 287 ° in azimuth. Four broad-band jammers are located about 100 to 200 km away at 5 ° or 10 ° in depression. Figure 9.4 shows the directions of the GPS signals and the locations of the jammers with respect to the receiver at the origin.

Assuming a typical noise power density of -204 dBW/Hz, the noise power is therefore -134 dBW for a 10 MHz bandwidth. The IQ data are scaled such that the noise in the data corresponds to the thermal noise. Given that the IQ data have a SNR of about 35 dB, the effective source power of all four jammers are calculated to be roughly 50 dBW. The GPS signals from four satellites are then added to the IQ data. The power of the GPS signals are assumed to be 10 dB below the noise power.

The performance of the space-time adaptive processors is measured based on the ratio of the SINR to the array-signal-to-noise-ratio (ASNR). The ASNR is simply 7 times the SNR for a 7-element array antenna. The SINR/ASNR will be 0 dB if there is no jamming or the effect of jamming can be completely eliminated. In computing the SINR, the array output is correlated with the original known sequence of ± 1. The peak of the correlation function, after being squared and appropriately scaled by the coherent gain, is the output signal power. Figure 9.5 shows the resulting correlation functions for the three algorithms with the peaks corresponding to the SINR/ASNR's.

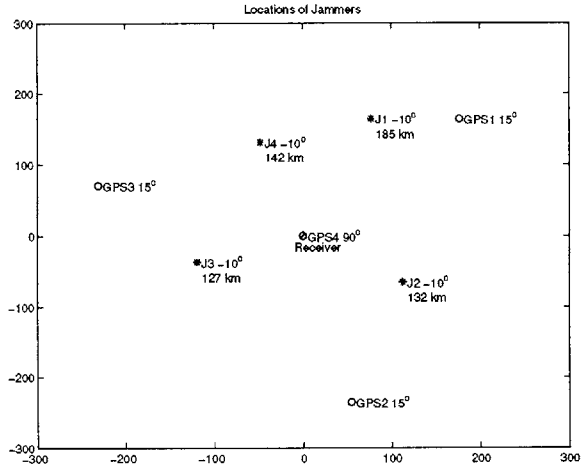

Figure 9.4: Jammers' Positions and GPS Signal Directions

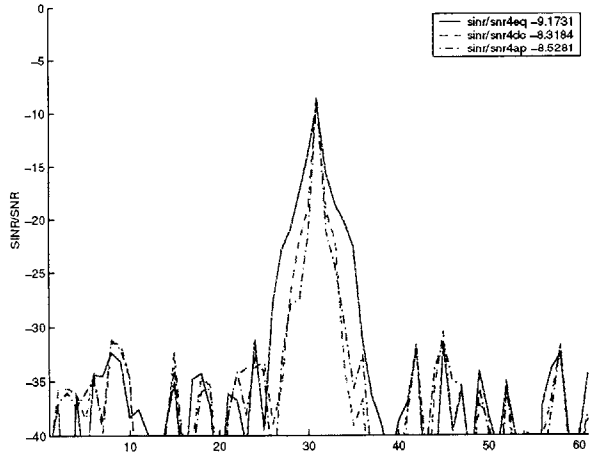

Figure 9.5: Correlation Peaks

The performance of a spatial-only structure (1 tap) is compared with the performance of a space-time structure with a delay line of 3, 5 and 7 taps. Comparisons are also made among the different algorithms as derived in Section 9.2. The following four tables, each corresponding to one of the four beams, show the average results for using different weight-constrained processors and varying number of taps.

GPS#1 - 15 ^{0}	Equalized	Delay Const.	All-Pass
Spatial	-27.9 dB		
3 taps	-20.1 dB	-19.4 dB	-21.9 dB
5 taps	-19.1 dB	-18.2 dB	-18.8 dB
7 taps	-18.9 dB	-17.4 dB	-17.3 dB

Table 9.1: SINR/ASNR for Satellite #1

GPS#2 - 15 ^{0}	Equalized	Delay Const.	All-Pass
Spatial	-23.0 dB		
3 taps	-18.6 dB	-16.9 dB	-18.3 dB
5 taps	-17.6 dB	-16.6 dB	-17.6 dB
7 taps	-17.4 dB	-16.4 dB	-17.0 dB

Table 9.2: SINR/ASNR for Satellite #2

GPS#3 - 15 ^{0}	Equalized	Delay Const.	All-Pass
Spatial	-22.6 dB		
3 taps	-21.5 dB	-20.1 dB	-21.0 dB
5 taps	-19.8 dB	-19.5 dB	- 19.9 dB
7 taps	-20.8 dB	-19.1 dB	- 19.3 dB

Table 9.3: SINR/ASNR for Satellite #3

GPS#4 - 90 ^{0}	Equalized	Delay Const.	All-Pass
Spatial	-20.3 dB		
3 taps	-16.4 dB	-15.1 dB	-15.8 dB
5 taps	-15.2 dB	-13.8 dB	- 14.3 dB
7 taps	-15.2 dB	-13.8 dB	- 14.0 dB

Table 9.4: SINR/ASNR for Satellite #4

The improvement going from a spatial-only processor to a 3-tap space-time processor is quite significant. Depending on the beam direction, the improvement can range from 3 to 8 dB for the given simulation set-up. The performance continues to get better as the tapped delay line is increased to 5 taps. However, the improvement going from 3-tap to 5-tap is only very small – about 1 to 2 dB typically. Going to a 7-tap processor, the increase in performance is no longer significant. The asymptotic limit in performance has been reached when the tapped delay line is about 5 taps.

The performance of different algorithms can be compared from the SINR/ASNR results. The equalization method shows the worst performance. The gain in SINR/ASNR is expected when a longer tapped delay line is used. For the equalization method, a longer tapped delay line would result in a longer equalization FIR filter for each beam. Two undesirable effects from using a long FIR can be observed. Firstly, the equalization FIR filter broadens the width of the correlation function as shown in Figure 9.5. Secondly, applying the FIR filter to the beam output may slightly corrupt the signal reducing its correlation with the original GPS sequence. For those reasons, the SINR for the equalization method is generally a couple dB's worse than the delay-constrained or all-pass techniques. The all-pass method is expected to perform much more poorly than the delay-constrained method due to the stricter requirement that the effective FIR must be an all-pass at a fixed group delay. It is seen from the simulation results that the all-pass SINR is actually only slightly inferior to the delay-constrained results. This difference in performance between the two constraints is much less than what expected in the theoretical analysis. Nevertheless, the delay-constrained algorithm is revealed to be superior to the other two methods for any number of taps.

10 Conclusion

In a jamming setting, a multi-element antenna array is used to form a beam steering toward the desired GPS signals. As the jamming signals interact with the airframe itself resulting in a near-field multi-path environment, space-time adaptive array processing is proposed as a method for more effective nulling of wide-band jammers. Using the actual experimental data, the multi-path phenomenon is characterized by forming space-time covariance matrices for all directions with respect to the aircraft. Based on those covariance matrices, simulated data can be generated for any number of jammers, desired directions, and power levels. Space-time adaptive processing techniques are then employed to recover the GPS signals embedded in the jamming data. It is found that a space-time processor performs significantly better than a spatial-only processor. This shows consistently with the eigenvalue spread that near-field multi-path scatterers are always present. The performance of three different algorithms are evaluated and compared with one another. The delay-constrained approach is seen to be the most effective.

The space-time adaptive processor is not an ideal processor without limitations. The seven-element array processor is only capable of dealing with up to 6 jammers. In a more severe jamming environment, the processor will not have enough degrees of freedom to null out all jammers simultaneously. For fewer jammers, the space-time processor will also fail to operate effectively when the jamming sources radiate more than 65 dBW within a 200 km radius. Other than those extreme conditions, the space-time adaptive processor can perform reasonably well in a jamming surroundings.

References

[1] Parkinson, B., and Spilker J., Eds.
Global Positioning System: Theory and Applications Vol 1.
Washington D.C.: American Institute of Aeronautics and Astronautics, Inc., 1996.

[2] Monzingo, R., and Miller, T.
Introduction to Adaptive Arrays.
New York: Wiley, 1980.

[3] Hatke, G.
"Adaptive Array Processing for Wideband Nulling in GPS Systems."
Proceedings of 32nd Asilomar Conference on Signals, Systems, and Computers, Pacific Grove, CA, Nov. 1998.

[4] Fante, R., and Torres, J.
"Cancellation of Diffuse Jammer Multipath by an Airborne Adaptive Radar."
IEEE Trans. AES, vol 31, no. 2, pp. 805-820, April 1995.

[5] Jablon, Neil K.
"Adaptive Beamforming with Imperfect Arrays."
Ph.D. Dissertation, Stanford University, Stanford, CA, Aug. 1985.

[6] Najm, W.,
"Constrained Least Squares in Adaptive, Imperfect Arrays."
IEEE Trans. AP, vol. 38, no. 11, pp.1874-1878, Nov. 1990.

[7] Shan, T., and Kailath, T.
"Adaptive Beamforming for Coherent Signals and Interference."
IEEE Trans. ASSP, vol. ASSP-33, no. 3, pp.527-536, June 1985.

[8] Er, M., and Cantoni, A.
"A New Approach to the Design of Broad-Band Element Space Antenna Array Processors."
IEEE JOE, vol. OE-10, no. 3, pp.231-240, July 1985.

[9] Hatke, G., and Schwartz, S.
"Soft Constrained LMS Algorithms: A Robust Procedure for Signal Misalignment."
Proceedings of 22nd Asilomar Conference on Signals, Systems, and Computers, 1989.

[10] Lin, S., and Barkat, M.
"The Performance of the SMI Method in the Constrained LMS Array and the Griffiths Array."
IEEE Trans. AP, vol. 38, no. 11, Nov. 1990.